Independent SAR System Calibration of Sentinel-1C

Patrick Klenk, Kersten Schmidt, Jakob Giez, Andrea Pulella, Matteo Nannini, Pau Prats-Iraola, Marco Schwerdt

***Abstract*—Sentinel-1C is the third satellite of the Sentinel-1 mission. Launched in late 2024, it ensures seamless continuity of C-band SAR data for global monitoring of the Earth surface in the framework of the Copernicus program. In parallel to the commissioning of Sentinel-1C by the European Space Agency (ESA), an independent verification of the system calibration has been performed by the German Aerospace Center (DLR) under an ESA contract. Based on an efficient calibration strategy, this paper describes the different activities performed and discusses in detail the results and main findings of DLR during the commissioning phase (CP) of Sentinel-1C. The main goal is to provide a comprehensive compendium of the SAR calibration and performance status of S1C at the beginning of its operational mission: At the end of the commissioning phase we find that S1C achieves or even exceeds all SAR performance requirements put forth and is ready for its nominal mission operations.**

***Index Terms*—Synthetic Aperture Radar (SAR), SAR Calibration, Interferometric Verification, Sentinel-1, Sentinel-1C, Copernicus, Radar, Earth Observation**

I. Introduction

The Sentinel-1 SAR mission comprises a constellation of radar satellites, developed, deployed, and operated within the framework of the joint European Commission(EC)/European Space Agency (ESA) Copernicus program (e.g., [1], [2], [3]). The goal is to continuously and comprehensively provide SAR imagery of the Earth's surface at C-band, operationally serving a plethora of different scientific and security related objectives and services.

To fulfill its revisit and coverage related requirements, the mission is nominally based on a constellation of at least two satellites which are designed for a nominal lifetime of five years (with consumables for an additional five years). The first, Sentinel-1A (S1A), was launched in spring 2014 and was joined two years later by its identical sibling, Sentinel-1B (S1B), operating at an 180 degree orbit phasing after conclusion of its commissioning phase. S1B has unfortunately suffered a non-recoverable anomaly related to the instrument electronics power supply in December 2021 and has in the meantime been put on a re-entry trajectory. Meanwhile, S1A has already been operating well beyond its nominal lifetime with increasing challenges to the execution of orbit control maneuvers. The gap in the satellite constellation left by S1B has finally been filled by Sentinel-1C (S1C) [4], which started its operational phase in May 2025 after five months of commissioning activities. S1A will be operationally replaced by the last unit of the first generation of Sentinel-1 satellites, Sentinel-1D (S1D) in mid 2026.

The multitude of different operational objectives for the Sentinel-1 mission has led to stringent requirements imposed on the SAR performance, requiring careful calibration of the SAR instruments both on ground and during in-orbit commissioning. To ensure the S1C SAR performance, DLR performed an independent calibration campaign of the S1C SAR system on behalf of ESA during the commissioning phase of the spacecraft, following a dedicated in-orbit calibration plan introduced and detailed in [5]. To provide for a maximally independent assessment of the S1C calibration, DLR has used own tools, procedures and most importantly our own ground reference targets as detailed further in section II, working independently of the Agency's commissioning activities to the furthest extent possible. The results obtained through this independent DLR campaign are presented in this paper, summarizing the calibration and verification tasks performed and discussing the S1C SAR performance at the start of its operational phase in May 2025.

This paper is organized as follows: First, sections II and III will briefly introduce the DLR SAR calibration Center, its support for Sentinel-1, and give an overview of DLR's calibration campaigns supporting S1 commissioning. The following Sections IV to XIII will then thoroughly discuss major results achieved during calibrating the S1C SAR instrument. We show (i) the internal calibration performance (Section IV), (ii) the radio-frequency characterization and monitoring (Section V), (iii) antenna pointing performance (Section VI), (iv) antenna-model verification results (Section VII), (v) NESZ performance (Section VIII), (vi) geometric, polarimetric and radiometric performance (Sections IX-XI), (vii) IRF quality analyses (Section XII), and a verification of the interferometric performance (Section XIII-A). Last but not least, we showcase some exemplary interferometric results (Section XIII-B) based on the S1A/C orbit phasing during the S1C commissioning phase, which allowed the unique opportunity to acquire 1-day repeat-pass interferograms over dedicated areas between S1C and S1A throughout the first phase of commissioning S1C.

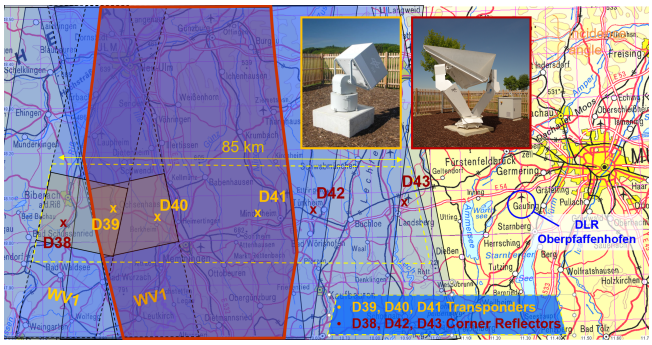

Fig. 1. S1 coverage overview for the different beams which can be acquired over the DLR calibration field.

The authors are with the Microwaves and Radar Institute, German Aerospace Center, Münchener Str. 20, 82234 Wessling, Germany. Corresponding Author: patrick.klenk@dlr.de

II. DLR SAR Calibration Center Support for Sentinel-1

During the past two decades, the DLR SAR Calibration Center [6] has been responsible for the overall SAR system calibration and validation concept for a range of different national and international SAR missions, including ESA's Sentinel-1 SAR mission program. All algorithms required for accurate calibration of the entire Sentinel-1 system have been developed by the Center during the Sentinel-1A definition [7] and adapted during the S1A/B implementation phases [8]. In the framework of the Sentinel-1C definition and implementation phase since 2016, this concept and the calibration algorithms have been adapted and developed further for S1C and S1D to cope with the challenge of novel instrument technology to achieve a smooth transition between all four satellites.

To adapt the DLR calibration facility to the increasing demands of modern SAR systems, DLR has been developing innovative and highly stable reference targets which are deployed at our calibration field in the South of Germany (e.g., [9], [10]). **Figure 1** shows an overview of the Sentinel-1 coverage of those targets. These targets (three remote controlled corner reflectors and three "Kalibri" transponders) have been in operation since early 2014, demonstrating their accuracy and reliability. Their fully remote-controlled operation, outstanding radiometric accuracy and their polarimetric capabilities have been playing a key role in the calibration and long term system monitoring activities for Sentinel-1 (e.g., [11], [12]).
At present, the Center also develops and builds transponders for supporting upcoming SAR missions in X-band and L-band (e.g., [13], [14]).

III. DLR's Independent SAR System Calibration Campaigns for S1

Due to the stringent performance requirements of Sentinel-1, on behalf of ESA, the DLR SAR Calibration Center performed an independent assessment of the end-to-end system calibration of S1A in 2014 ([15], [16]) and of S1B in 2016 [17], relying on a separate dedicated suite of in-house analysis tools. A detailed in-orbit calibration plan was derived, and innovative reference targets were designed, manufactured and deployed. Based on the different calibration activities performed by the DLR Calibration Center, an independent calibration of both satellites S1A and S1B could be achieved during the respective commissioning phases. Since then, the DLR Calibration Center has been also involved in monitoring and improving the calibration of both systems during routine operations on behalf of ESA (2014 – 2019) and as member of the Mission Performance Center (MPC) Team on behalf of CLS since 2019 (e.g., [11], [12], [18]).

Based on the success of these calibration campaigns for the preceding S1 SAR instruments, DLR has now performed an independent calibration campaign for S1-C on behalf of ESA [5], with the comprehensive results detailed and discussed in the following sections, as described above. Most of the data has been acquired over seven repeat cycles of the nominal S1C SAR instrument commissioning activities between January 17th and April 30th 2025, after the spacecraft had reached its commissioning orbit. These seven repeat cycles have been split into two different phases. For the first four repeat cycles, S1C was operated in a 30° orbit phasing to S1A, leading to a one-day exact repeat with S1A. Before the fifth repeat cycle (early to mid-March), the spacecraft was repositioned to its operational orbit node with a 180° orbit phasing (i.e, the nominal six day repeat) with respect to S1A. The unique orbit phasing for the initial cycles were mainly used for S1A/C cross-interferometric purposes as discussed further in Section XIII, while the drift phase was used to apply already some on-board corrections derived from first phase acquisitions, such as an attitude correction for the elevation pointing bias (see Section VI-B).

IV. Internal Calibration

Temperature variations and internal hardware characteristics affect the radar signal path, resulting in gain and phase fluctuations during data acquisition. These variations arise from thermal effects, hardware degradation, or extreme space conditions. To monitor and compensate for such changes, an advanced internal calibration strategy was developed for Sentinel-1C as for its predecessors 1A/B. This strategy uses different types of internal calibration measurements, leakage suppression algorithms, and the pulse-coded calibration (PCC) method [19]. These pulses are generated at the SAR Electronics Subsystem (SES), routed via the distribution network to the tile amplifiers (TA) and to the front-end (EFE), coupled out at the calibration coupler located in the EFEs and sent back to the receive chain in the SES.

Calibration pulses matching the imaging data settings are used to retrieve replica with imaging settings, while 100 MHz full-bandwidth calibration pulses support long-term instrument drift analysis and transmit/receive module (TRM) characterization (see Section V). However, these internal calibration pulses are affected by coherent, phase-modulated leakage signals. To mitigate these degradation effects and ensure instrument stability, specific correction algorithms are applied to the calibration data [20]. Furthermore, instrument time delay must be accounted for to correct the uncertainty introduced by the analog-to-digital converter (ADC), as the on-ground

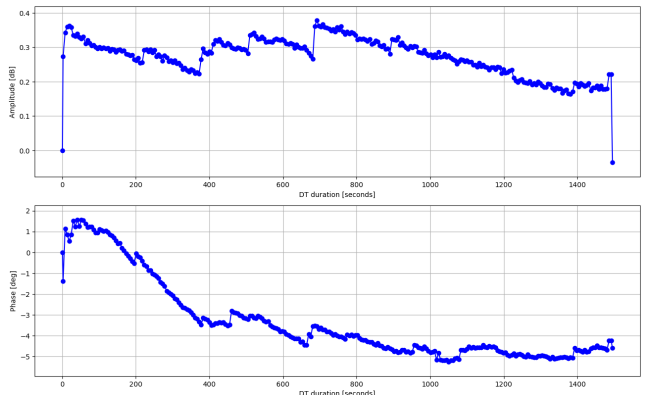

Fig. 2. S-1C instrument drift over an extra long data take acquired in December 2024

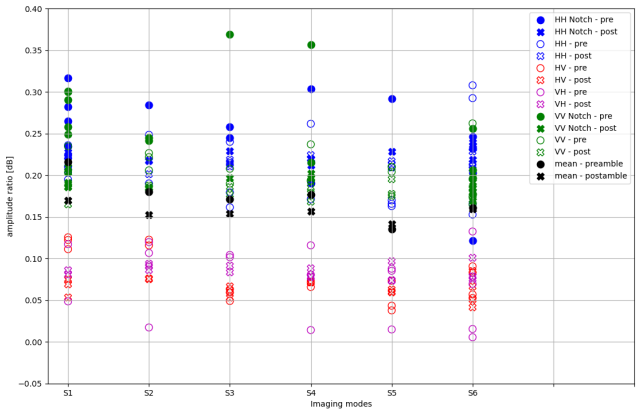

Fig. 3. Offsets extracted from S-1C products between preamble and first interleaved sequence (dots), as well as the last interleaved and the postamble (crosses). The different colors represent the polarization.

processor assumes an adapted ideal chirp for SAR data range compression.

In comparison to its predecessors Sentinel-1A/B, the updated instrument architecture of Sentinel-1C allows for a reduced number of three (Tx, Rx and EPDN), instead of five calibration pulses, each one being routed through a different part of the RF path [21]. This change has impacts on the whole calibration process, since all calibration algorithms are based on those signals, hence required to be adapted and verified.

A. *Instrument Stability*

In order to provide a high precision for SAR acquisitions, the instrument drift during data takes needs to be compensated for. For Sentinel-1 the instrument drift monitoring for amplitude and phase is done by analyzing the replica, which is represented by the Power-Gain-product (PG-product) for Sentinel-1. The PG-product can be generated using all three calibration signal types from the same calibration sequence, which is shown in eq.1. It thereby represents all RF components that the actual SAR signal passes through, with TXCal representing the transmit path, RXCal the receive path and EPDNCal the contributions of the calibration path. In order to properly monitor the drift induced by the thermal fluctuations during the data takes, the replica is calculated from the 100 MHz full bandwidth sequences, that are available over the full data take. Amplitude and phase drift can then be monitored by normalizing the replicas to the amplitude and phase values of the first sequence.

$$\mathrm{PG}_{\mathrm{product}}(n) = \frac{\mathrm{TXCal}_{\mathrm{polTX}}(n) \cdot \mathrm{RXCal}_{\mathrm{polRX}}(n)}{\mathrm{EPDNCal}_{\mathrm{polTX}}.(n)} \qquad (1)$$

During the commissioning of Sentinel-1C the instrument showed high stability even for very long data takes with durations of close to 25 minutes and temperature variations of approximately 20° C in the electronic front end. Exemplary, the drift values of an extra long IW data take can be seen in **Figure 2**. With an instrument drift in amplitude of 0.31 dB and phase of 4° C over the full data take the instrument proves the high precision with an approximate drift of only 0.013 dB/min and 0.162°/min in amplitude and phase. The drift measured by the calibration pulses is compensated during on ground processing. Thus, the remaining instrument drift can be kept at a low level below 0.1 dB in amplitude and only a few degrees in phase. A closer look at Figure 2 reveals an offset between the first and second amplitude values, or the penultimate and last amplitude values, at the beginning and end of the data take. This offset between pre- and postamble sequences and interleaved sequences is compensated for in data takes with interleaved sequences by the drift compensation. However, in most stripmap modes, there are no interleaved sequences since the recording is continuous. In these cases, the correction values are interpolated using the pre-/postamble values. To compensate for the error caused by the offset, a dedicated campaign with special stripmap acquisitions containing interleaved calibration pulses was conducted for Sentinel-1C to characterize the average offsets. Results are shown in **Figure 3**. Overall averaged offset values are provided in **Table I**. As can be seen the correction values differ for co-polar and cross-polar recordings with 0.2 dB and 0.08 dB, respectively. Thus, separate correction values for co- and cross-polar channels have been introduced, which can be applied directly to the abs cal factor.

TABLE I
OVERALL AVERAGED PG OFFSETS FOR SM ACQUISITIONS.

	HH-pol [dB]	VV-pol [dB]	HV-pol [dB]	VH-pol [dB]
SM-preamble	0.207	0.208	0.079	0.073
SM-postamble	0.215	0.180	0.065	0.084
SM-co/cross	**0.203**		**0.075**	

B. *Imbalances and Data Take Normalization*

In addition to providing sufficient stability within one data take and for a single polarization, another important aspect of the internal calibration is monitoring the performance in between different data takes and the two receiving polarizations. The monitoring is again based on the replica. The values of the

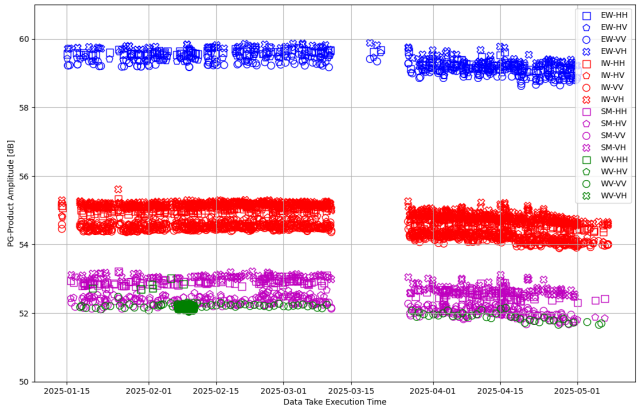

Fig. 4. S-1C PG-product in amplitude over the full commissioning phase. The different image modes are highlighted by the colors (EW, IW, SM, Wave) and the different signs represent the product polarization.

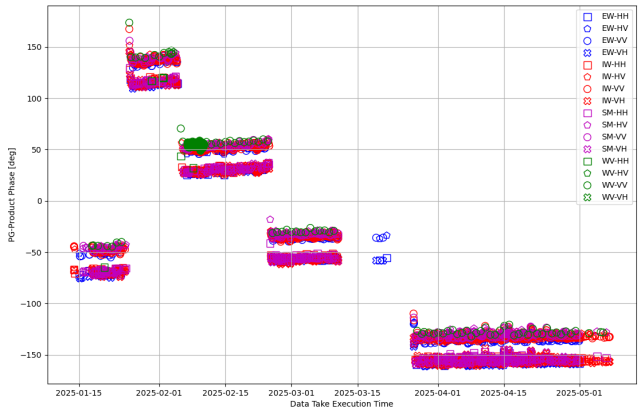

Fig. 5. S-1C PG-product in phase over the entire commissioning phase. The different image modes are highlighted by the colors (EW, IW, SM, Wave) and the different signs represent the product polarization.

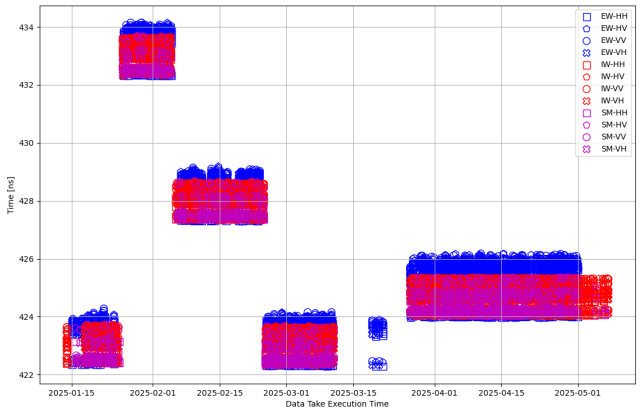

Fig. 6. S-1C internal delay over the full commissioning phase. The different image modes are highlighted by the colors (EW, IW, SM) and the different signs represent the product polarization.

mean amplitude and the mean phase for each data take over the full commissioning phase can be seen in **Figures 4** and **5**, respectively. For the inter channel imbalance corrections the offset is derived from the first 100 MHz calibration sequence located at the data take preamble. The inter channel imbalance can either be derived from the replica as suggested by the manufacturer [21] or the RX-Cal pulse only, as polarimetric differences of TX-Cal and EPDN-Cal pulses are considered negligible. The imbalance itself can be seen in the amplitude (Figure 4) and phase (Figure 5) plot as the offset between the two groups, representing the H-polarization (cross and square) and the V-polarization (circle and pentagon). The values vary between 0.24 dB and 0.63 dB in dual polarization with V-polarization in transmit and 0.03 dB to -0.38 dB in dual polarization with H-polarization in transmit. This leads to the conclusion that in general the H-polarization channel has a stronger gain in receive than the one in V-polarization and additionally, V-polarization has an approximately 0.25 dB stronger transmit gain than H-polarization. For Sentinel-1A/B these imbalances had been pre-corrected based on Ground Characterization (OGC) results. Nevertheless, the observed channel imbalances have no influence on the final SAR-product as the difference between the polarization channels remains stable and hence this offset can be fully compensated by the PG-product.

The data take normalization between multiple data takes is performed by comparing the mean maximum of the replica over one data take to one reference factor defined at the beginning of the commissioning phase. The comparison is hereby done for each polarization, imaging mode and subswath separately with its corresponding reference factor. As can be seen in both PG plots over time the amplitude and phase values stay extremely stable over the full commissioning phase. One jump can be seen in amplitude and phase after the drift phase in the middle of March, where the satellite was moved to its final orbit position. A slight drift of the amplitude values can be noticed in the second half of April which stabilizes afterwards. This is most likely connected to the failure of two TRM in tile 14 during that timeframe (cf. sectionV-B. In addition, four jumps are visible in the internal instrument delay. All jumps were expected and are connected to instrument switch offs, which also affect the analog to digital converter (ADC) and therefore the phase locked loop (PLL).

Another parameter that needs to be monitored over the commissioning phase and gives an indication of the instrument stability is the internal instrument delay. The internal instrument delay is required for processing a Sentinel-1 image since the range compression is performed by an ideal chirp that needs to be shifted by the time delay to consider the ADC uncertainty of the system. The internal delay is derived from the replica and an ideal chirp and can be seen in **Figure 6**. As can be seen the offset stays extremely stable over the full commissioning phase with no visible drifts. Since the internal delay is directly derived from the replica, which is represented by the PG-product for Sentinel-1, the same jumps as in the PG-phase (Figure 5) can be seen in the internal delay.

V. TRM Characterization

Sentinel-1 is equipped with an RF Characterization (RFC) mode, an efficient technique for analyzing the individual signal paths of its active phased array antenna, alongside with each paths dedicated Transmit/Receive Module (TRM). This mode employs the Pulse Compression Calibration (PCC) method, also known as the PN Gating technique [19]. With this approach, an individual excitation coefficient for each TRM can be deduced, thus making a TRM-wise monitoring possible.

To monitor variations in these excitation coefficients, such as long-term drifts or hardware failures, an error matrix is introduced. The error matrix contains deviations values, calculated from excitation coefficients based on recent data takes and a defined reference as is shown in eq. 2, with g being the amplitude values, Φ the phase values and p the number of the data take:

$$\Delta\mathrm{TRM}_{\mathrm{p}}(\mathrm{trm},\,\mathrm{tile}) = \frac{g_{\mathrm{p}}(\mathrm{trm},\,\mathrm{tile})}{g_{\mathrm{ref}}(\mathrm{trm},\,\mathrm{tile})} \cdot e^{j(\Phi_{\mathrm{p}}(\mathrm{trm},\,\mathrm{tile})-\Phi_{\mathrm{ref}}(\mathrm{trm},\,\mathrm{tile}))}. \quad (2)$$

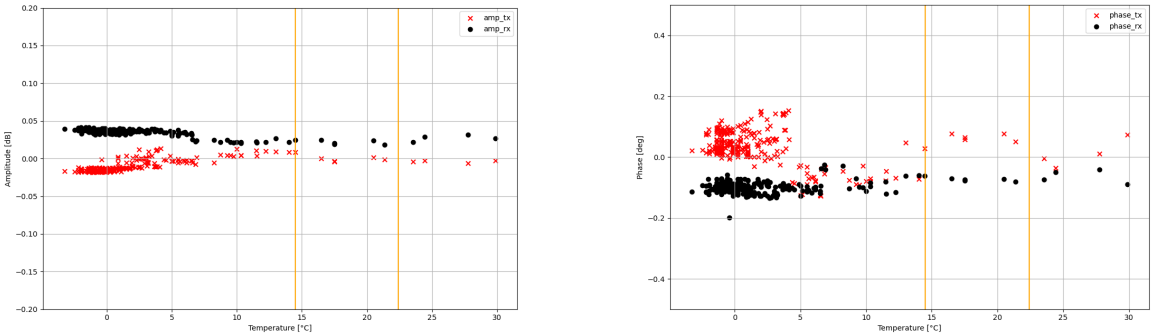

(a) (b)

Fig. 7. S-1C H-polarization excitation coefficients from 24 hour campaign in December 2024 as mean value over all 240 TRMs over the mean antenna temperature, with amplitude values in 7a and phase in 7b.

The reference g_{ref} can be based on the initial set of excitation coefficients configured during system setup, a set derived by averaging multiple measurements taken during OGC or in-flight RFC measurements during the CP. For S1C the latter option is employed, as described in the following.

A. Reference Matrix Generation

On December 14th, a 24-hour RFC campaign was conducted using Sentinel-1C. RFC acquisitions were performed continuously in both transmit polarizations to monitor the front-end status and assess its stability across varying operational temperatures.

Furthermore, a subset of RFC measurements from this campaign was selected to establish new in-flight TRM reference values. These measurements were chosen based on instrument temperatures during the OGC phase, specifically in the range of 14° C to 21° C. In line with manufacturer recommendations, six RFC acquisitions in H-polarization and six in V-polarization within this temperature range were selected. The average of these measurements was used to define the new in-flight reference excitation coefficients.

Figure 7 displays the mean excitation coefficients of the full antenna over individual data takes, plotted against the mean EFE temperature. The temperature range relevant to the OGC is indicated with orange bars, enclosing the six data takes per polarization. All excitation coefficients show a very stable performance and are therefore well suited as base for a reference matrix.

B. Long Term Stability Monitoring

The antenna health monitoring was conducted over the full commissioning phase for both polarizations and transmit paths. Furthermore, the antenna was monitored on tile and TRM level to cover all possibly occurring drifts and failures. The matrix described in section V-A was hereby taken as reference to guarantee high precision and sensitivity to changes. Due to an interference with the temperature compensation, the Tx-Cal coefficients are normalized by the corresponding EPDN coefficient. **Figure 8** shows the deviations derived for each of the 14 tiles, each as average over its 20 individual TRMs in H-polarization. The black line represents the mean deviation across all 280 TRMs, indicating the average offset from the reference values derived from in-flight averaged RFC data.

The plots show a highly stable performance over the commissioning phase, with the Rx-chain deviations showing higher deviation values in general than the Tx-chain values. The amplitude deviations stay within 1 dB and phase deviations below 10°. Only minimal drift behavior is observed in a few cases, e.g. for Tile 8 in transmit H-polarization. Additionally, a step-like change in both amplitude and phase is visible following the drift period in the middle of March. The most significant change in the antenna could be detected in Tile 14 at the end of April as a result of the failure of two TRM in both signal paths and both polarizations.

Figure 9 illustrates the deviations of all 280 individual TRMs in the front-end relative to their reference values throughout the full CP. Each green dot represents an evaluated RFC measurement taken between January and May 2025. The black line indicates the mean deviation for each TRM, representing the average offset from the reference.

Clear anomalies are visible in TRM3 and TRM4 of Tile 14 (units 263 and 264), indicating the prior mentioned failures in those modules. Notably, higher amplitude deviations in this case are observed in Tile 3, 8 and 11, though their standard deviation remains within normal limits, and thus they are not considered critical.

VI. Antenna Pointing

Antenna pointing calibration is a major task for ensuring a correctly aligned SAR antenna radiation pattern. This combines both the correct measurement and control of the attitude of the satellite as well as the electronic adjustment of the SAR antenna. Correct pointing is required to illuminate the acquired swaths with maximum signal power, as the antenna patterns are designed exactly for this purpose. The procedure of determining the antenna pointing for S1C is divided into two parts: (i) azimuth antenna pointing and (ii) elevation antenna pointing with the respective results discussed in the following two sections.

To orient itself in space, Sentinel-1C has a three star-tracker system, two of which are in operation concurrently

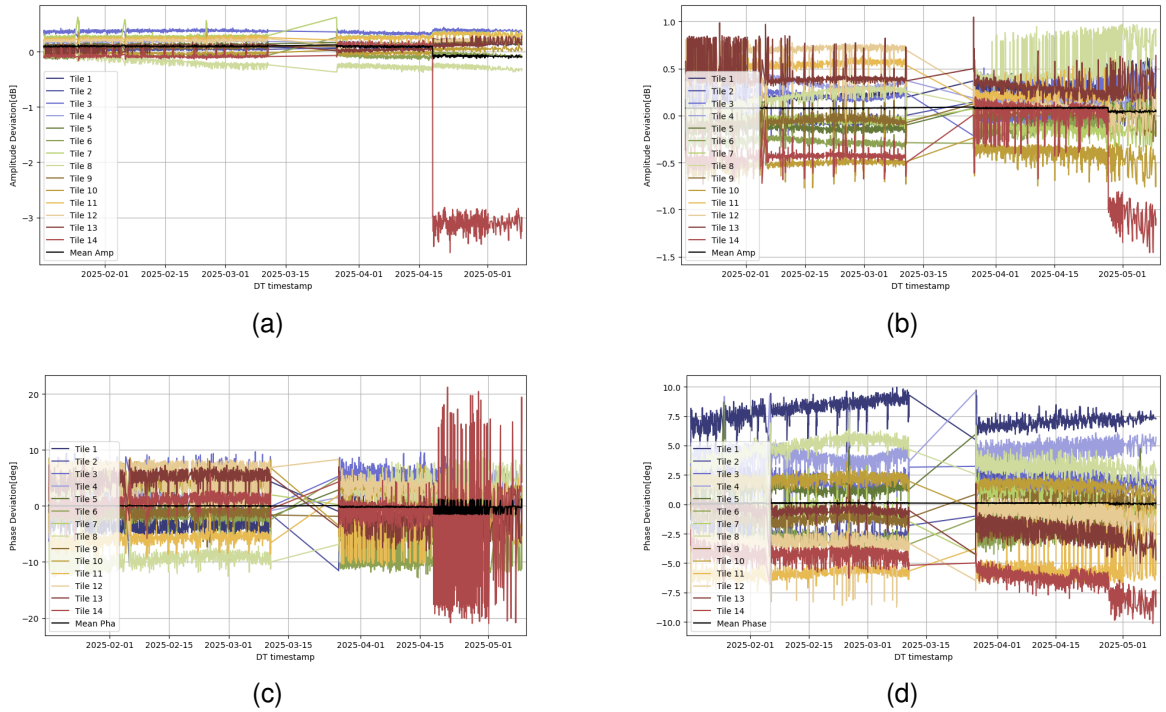

Fig. 8. S-1C Excitation coefficients deviations for H-pol over full commissioning phase with visible TRM failure in April 2025 (TRM 3+4 of Tile 14).

at each time. After launch, a relative alignment of these star-trackers has to be executed in order to minimize the platform pointing differences between the different combinations and in turn the impact on the SAR antenna pointing. For S1C, (i) this star tracker inter-alignment between the different possible star tracker combinations was already completed before the start of SAR instrument commissioning, and (ii) SAR acquisitions throughout the S1C commissioning phase were acquired in pre-defined phases in which the different star tracker combinations were active. This allowed us also to test the efficacy of the pre-cycle-1 star-tracker inter-alignment through dedicated measurements with different active star-tracker combinations. Most pointing measurements have been acquired with star-tracker combination 1+2, which is also the combination intended for the operational phase with spot checks in combinations 1+3 and 2+3: Data until early February 2025 have been acquired with STT 1+2 being active, in early March with STT 1+3, late March 2+3 before switching back to 1+2 for the last measurements in April.

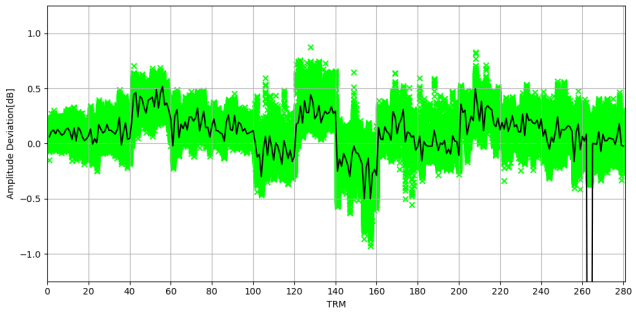

Fig. 9. S-1C Excitation coefficients deviations for TX-cal H-pol over full commissioning phase with visible TRM failure in April 2025 (TRM 3+4 of tile 14).

A. Azimuth Pointing

For the pointing determination in azimuth, we used transponder recordings of so-called notched patterns to measure the pointing in azimuth. For this purpose, the transponder records the transmit pulses of the SAR system as a function of time, while the SAR instrument is commanded to transmit an azimuth notch, i.e. a distinct minimum feature in the center of the main beam along the azimuth direction. A comparison between the notch position measured by our transponders and the notch position which would be expected from corresponding antenna model (AM) calculations yields an estimation for the antenna mispointing for a certain antenna look angle. As an example, **Figure 10a** shows one of these measurements for the N1 datatake acquired on 2025/01/22. The antenna model prediction is drawn in blue, whereas the three transponder measurements are depicted in red, green and black, respectively. Throughout the commissioning phase, different notch beams were measured, some of which also with different active star tracker combinations. The combined results are shown plotted over elevation in **Figure 10b**, with the initial six acquisitions (STT 1+2) drawn as circles, STT 1+3 acquisitions in diamonds and STT 2+3 in triangles.

From these measurements, we can observe:

- An overall very small AZ pointing bias, especially compared to Sentinel-1B, where the initial mean value was found to be between 20 and 30 mdegs [17]. For Sentinel-1C in comparison, there is almost no AZ mispointing

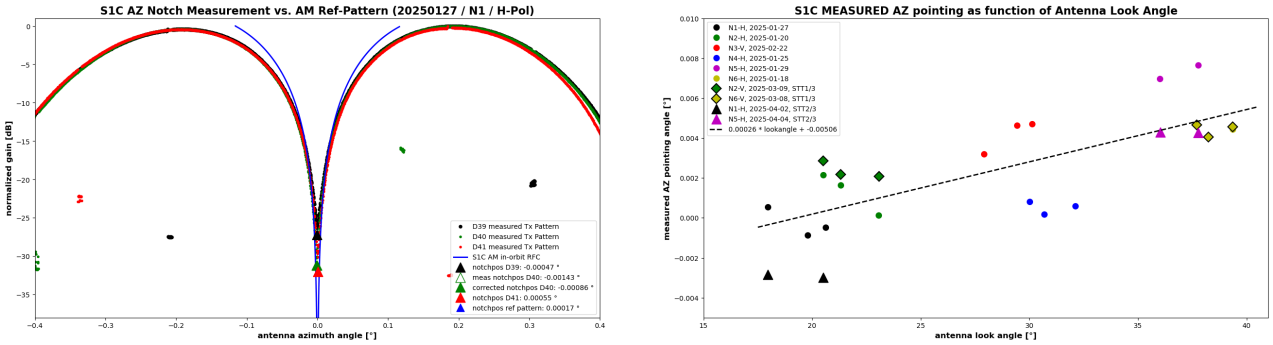

(a) (b)

Fig. 10. S1C azimuth pointing measured over DLR transponders: (a) Exemplary AZ notch measurement in N1-mode / H-Pol, recorded by three transponders (green, black and red dots) in comparison to the antenna model prediction (blue line), (b) all AZ pointing values retrieved over elevation including a linear fit to the data (black dashed line)

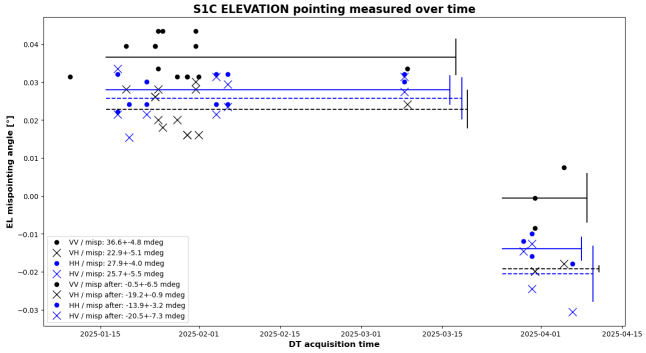

Fig. 11. Evolution of measured elevation pointing based on rainforest notch measurements throughout the S1-C commissioning phase.

observable for near-range beams while the value increases to a few mdegs in far range.

- A pointing dependency on antenna look angle is detected with a slope of about 0.2 mdegs / degree in lock angle. This points to a small misalignment of the instrument with respect to the spacecraft both in yaw and in pitch, which has been proposed to be corrected for accordingly.
- There is very little impact when different star tracker combinations are active, indicative of a successful inter-alignment before pre-SAR instrument commissioning and a huge improvement to what was observed for Sentinel-1B [17].

B. Elevation Pointing

Pointing determination in elevation also followed the same approach discussed in [17], calculating AZ-averaged, so-called range-profiles of data acquired over a homogeneous natural target (Amazon rainforest). For these acquisitions, the instrument is commanded with a notch in the elevation direction. Applying the relation between σ_0 and γ_0, the corresponding averaged gamma profile can then be extracted (both co- and crosspolarized channels have been considered). A polynomial fit to the central part of the measured notch allows to extract its minimum position, which is then compared to minimum position in the respective reference antenna pattern as calculated by the antenna model. The evolution of the thus derived elevation mispointing over all data acquired during the S1C commissioning phase is shown in **Figure 11**.

We observe:

- Initially a total elevation mispointing of approximately -30 mdeg,
- a polarization dependency of the elevation pointing with VV-Pol yielding larger mispointing results compared to the other polarization combinations,
- only slim-to-none dependency of the observed pointing with respect to the STT combination in operation, similarly to the AZ mispointing discussed in the previous section.

During the drift phase of the S1C S/C to its final orbit node in March 2025, an on-board roll-angle correction of -40 mdeg was carried out by the Agency. From measurements acquired after this correction, we can confirm the relative accuracy of this correction with mispointing values measured after the roll correction differing about -42 mdeg from the previously derived values. Detail figures are provided in **Table II**, showing that the current best estimate of the elevation pointing based on EN measurements is now -14±5 mdeg.

TABLE II
AVERAGED ANTENNA ELEVATION MISPOINTING VALUES DERIVED FROM ELEVATION NOTCH MEASUREMENTS

Polarization	before roll correction $\mu[m] \pm \sigma$[mdeg]	after roll correction $\mu[m] \pm \sigma$[mdeg]
HH	28 ± 5	-14 ± 5
HV	26 ± 5	-21 ± 3
VV	37 ± 4	-1 ± 7
VH	23 ± 5	-19 ± 1

At the S1C IOCR, we therefore recommended a fine-tuning of the absolute elevation pointing as well as the pointing offset between the polarization channels by shifting the corresponding reference patterns derived by the antenna model according to the differences observed in Table II.

VII. Antenna Model Verification

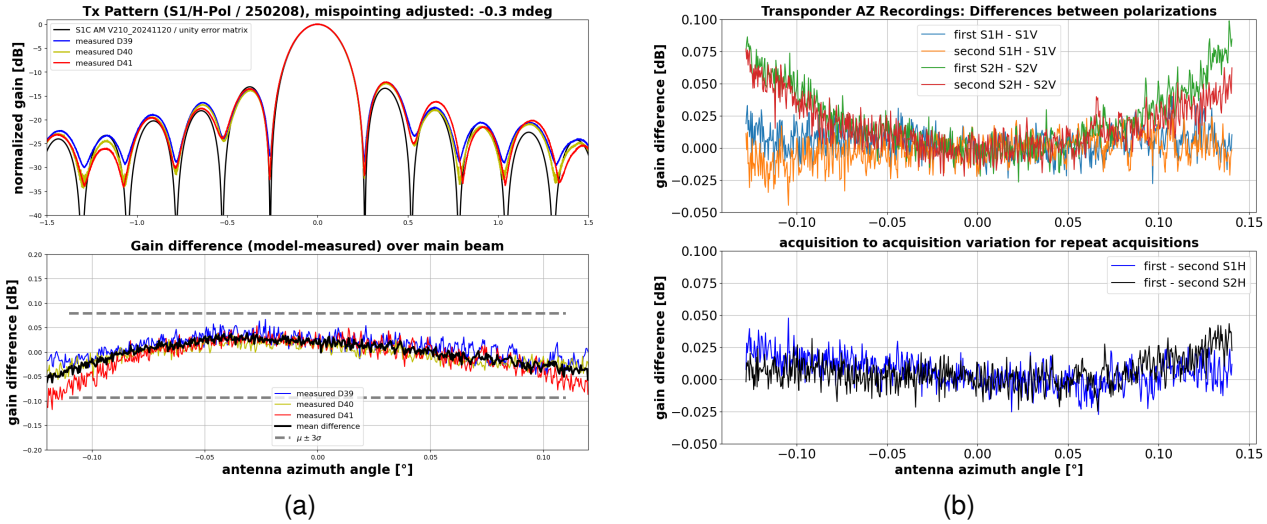

Fig. 12. Azimuth pattern verification: (a) Measurement for S2 on 2025-02-08, shifted by -0.3 mdeg to coincide at the maximum of the main beam. Above, plot across azimuth angles, below measurement/model difference over main lobe area for all three transponders (blue/yellow/red), with the mean deviation to the reference in black; (b) Top: Differences of averaged measurements for acquisitions with different polarizations. Bottom: differences of averaged measurements for repeated acquisitions

An accurate antenna model (AM) is a key element for the successful calibration and precise operation of a SAR system. Usage examples include the calculation of reference antenna patterns for correcting the impact of the antenna effects during SAR processing and the prediction of the relative gain differences between different subswaths for multi-beam modes (”beam-to-beam offsets”). In the following two sections, we therefore discuss the comparison of the patterns measured for S1C in-flight with those predicted by the S1C antenna model, first along azimuth (section VII-A) and then along elevation (section VII-B). For this antenna pattern verification, the nominal antenna beams and excitation coefficients are applied.

A. AM verification in Azimuth

Antenna model verification along azimuth follows the same measurement principle as for azimuth pointing determination: We record the one-way transmit pattern by the DLR transponders, but now for different nominal SM modes and compare the measured pattern in each case to the respective antenna model prediction. For more details on the methodology, refer to [17]. One exemplary result is shown in **Figure 12a** for an S1/H-Pol acquisition recorded on 2025/02/08. The upper graph of the figure depicts the measured patterns (in blue, yellow and red) recorded by each transponder, as well as the calculated reference patterns (solid black line). In the lower part of the figure, the difference between the reference pattern and the measured patterns is shown in the same respective colors, with the averaged difference drawn in black.

The results for all measured stripmap beams are summarized in **Table III**. For all cases, the deviation between measured modeled transmit patterns is less than 0.04 dB (1σ). Lowest average deviation has been measured for S5/H-pol with only 7 thousandths of a dB. We also note that only a minimum AZ pointing correction of less than 1 mdeg was necessary in each case to achieve the best overlap of the main-beams, corroborating the excellent S1C AZ pointing results discussed in section VI-A.

As evident from the table, for S1/H-pol and S2/H-pol, two acquisitions could be carried out in each case, spaced two cycles apart. Comparing the results of both acquisitions in **Figure 12b** (upper plot), we find an excellent repeatability of our transponder measurements with measured differences with respect to the antenna model being virtually identical in both cases, also indicating a stable antenna pattern performance of the SAR instrument over those two cycles. Furthermore, from comparing acquisitions acquired for the same stripmap beam at different polarizations (lower plot in the same figure), we see that the differences are also quite small. Especially for S1, the results are basically the same. For S2 a slight parabolic shape can be observed, this is due to the fact that the AM seems to be predicting the width of the pattern slightly better for H-Pol than for V-Pol in this case.

B. AM verification in Elevation

The in-flight verification of antenna elevation pattern is based on the same calculation of range gamma profiles as the elevation pointing verification described in section VI-B, now using nominal imaging acquisitions ([17]). For strip map beams (not shown), gain variations over elevation remain less than 0.15 dB (1 dB) for S1C in each case. Results for IW are pictured in **Figure 13**, comparing the averaged measured IW data to the corresponding antenna model prediction after applying a mispointing correction of 30 mdeg according to the elevation mispointing results derived in section VI-B.

Apart from the largely flat profiles, the figure shows that for S1C, initial beam-to-beam offsets are much reduced compared to S1A/B (shown, e.g., in [17]). The largest offsets are around 0.1 dB with overall gain variation in elevation remains within 0.3 dB (1σ). For EW acquisitions, finding data which can be

TABLE III
OVERVIEW OF ALL RESULTS ACHIEVED FOR STRIPMAP AZIMUTH PATTERN VERIFICATION

measurement date	swath	transmit polarization	applied pointing shift [mdeg]	AM - measurement difference over main beam / 1σ [dB]
2025/02/01	S2	H	-0.5	**0.029** (3 transponder average)
2025/02/08	S1	H	-0.3	**0.038** (3 transponder average)
2025/02/13	S2	V	-0.5	**0.040** (3 transponder average)
2025/02/20	S1	V	-0.8	**0.032** (2 transponder average)
2025/02/25	S2	H	0.0	**0.024** (3 transponder average)
2025/03/04	S1	H	-0.3	**0.033** (3 transponder average)
2025/03/06	S5	H	-0.2	**0.007** (3 transponder average)
2025/04/16	S5	V	0.2	**0.017** (2 transponder average)

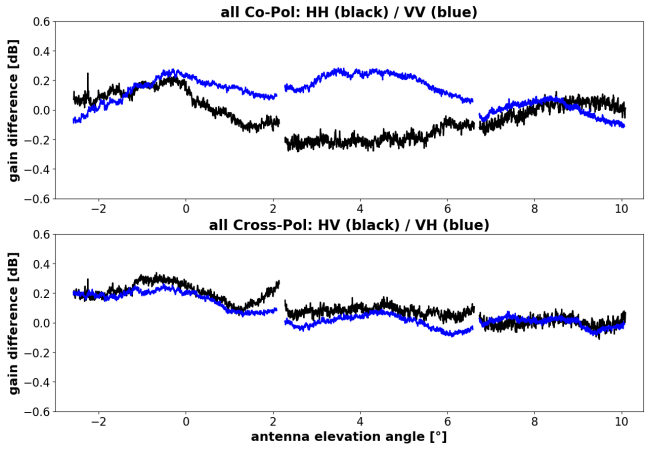

Fig. 13. Difference between averaged measured IW data after roll mispointing correction and the corresponding antenna model prediction. Co-Pol profiles are shown on top, cross-pol on the bottom.

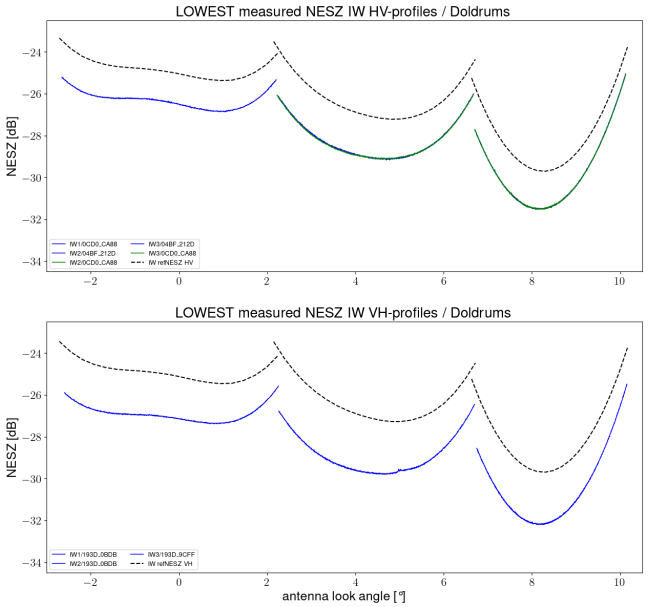

Fig. 14. Lowest NESZ profiles measured for S1C in IW mode over the doldrums for HV (top) and VH (bottom) channels. Blue lines show the lowest profile determined by overall mean value. For cases where selection by lowest overall value yielded a different profile, this is drawn in green. The black dashed lines indicate the design expectation from the S1A/B generation.

considered largely homogeneous rainforest presents an ever-larger challenge. From the data evaluated during the S1C CP, we found beam-to-beam offsets of up to around 0.2 dB (not shown).

VIII. NESZ VERIFICATION

Noise Equivalent Sigma Zero (NESZ) is a measure of the sensitivity of a SAR instrument. It describes the system noise superimposed with the inverted antenna pattern, which is applied during SAR data processing. Thus, NESZ analysis is performed to achieve an assessment of the sensitivity of the instrument and the correct application of the antenna pattern. For this purpose, distributed targets with extremely low σ_0-values are preferable, which by convention in X- and C-band is usually the Doldrums, a low-wind area in the Pacific Ocean. To ensure even less influence of potential residual backscatter, we only evaluate the cross-pol channels (HV and VH) respectively. Furthermore, repeated measurements have been carried out throughout the whole commissioning phase. For comparison against the expected design curves, the profiles with the overall lowest measured values were chosen. **Figure 14** shows exemplary results achieved in IW mode. Achieved mean values are compared against the expected design values for all S1 modes in **Table IV**, illustrating that the NESZ performance exceeds the design for all measurement modes. Especially for the operationally most used IW mode, the sensitivity is about 1.5 to 2.5 dB better than what was originally designed for S1A/B and a clear improvement over sensitivities measured for the first two Sentinel-1 instruments. This illustrates the success and efficacy of the hardware improvements implemented for the S1C/D generation, detailed, e.g., in [22] or [23].

IX. GEOMETRIC CALIBRATION

Precise geometric calibration is fundamental to the reliable exploitation of SAR imagery, as it enables the accurate mapping of SAR images onto the Earth's surface in two spatial dimensions: azimuth (along-track) and range (across-track). For this task, accurately surveyed corner reflectors are used as reference point targets. The annotated azimuth and range timing information extracted from the SAR image products is compared against the predicted timing from geometry using precise orbital parameters and the geometric relationship between sensor and reference target including additional corrections from the SAR instrument (internal delay) and atmospheric propagation delays.

TABLE IV
NESZ RESULTS COMPARED AGAINST THEORETICAL EXPECTATIONS

measurement mode	HV difference to expectation [dB]	VH difference to expectation [dB]
S1	-0.35	-0.51
S2	-0.96	-0.76
S3	-0.18	-0.37
S4	-0.29	-0.75
S5	-1.06	-1.59
S6	-0.29	-0.71
IW1	-1.48	-1.98
IW2	-1.94	-2.52
IW3	-1.70	-2.35
EW1	-2.10	-2.16
EW2	-2.13	-2.79
EW3	-1.95	-2.77
EW4	-1.68	-2.65
EW5	-1.24	-1.94

The geometric accuracy of SAR measurements relies on three key factors: the precision of the satellite's orbit, the accuracy of the surveyed point target positions, and the accuracy of corrections applied for the propagation path. The distance between the SAR sensor and each point target is determined based on their known positions, which were measured using differential GPS techniques, achieving an accuracy of a few centimeters. For the satellite's position, restituted orbit files (AUX_RESORB) are used. These files are available as near real-time (NRT) products within approximately 30 minutes of acquisition and provide a 3D positional accuracy of about 10 cm, as documented in [24]. Note, according to the Sentinel-1 Product Definition [25], the absolute location accuracy is defined using NRT orbits with 2.5 m for Stripmap and 7 m for IW mode; for the coarse resolution EW mode this parameter is not specified.

To account for continental drift, all geographic coordinates were referenced to the International Terrestrial Reference Frame (ITRF) 2008. Atmospheric delay corrections are dominated by the precision of the zenith total delay values, which are obtained from external meteorological or GNSS-derived sources which are provided by the European Geodetic Reference System (EUREF).

In order to avoid additional error sources related to the reference targets, which could potentially arise from active electronic components within the transponders, only corner reflectors are used for the geometric calibration as passive targets do not incur internal delays.

A. Pixel Localization Accuracy in Azimuth

To assess the pixel localization accuracy in azimuth (i.e., along the satellite's flight direction), an offset measurement is performed by comparing the timing of the target's closest approach to the satellite—corresponding to the Zero-Doppler plane—with the azimuth time at which the same target is annotated in the corresponding SAR image. This azimuth time shift Δt_{az} is then converted into a spatial offset Δx (in meters) by multiplying it with the satellite's ground velocity v_g.

$$\Delta x = \Delta t_{az} \cdot v_g. \tag{3}$$

Since SAR image annotations relate to Zero-Doppler geometry, an additional range-dependent correction is applied to accurately determine the azimuth offset. This bistatic correction $\delta t_{az}^{\text{bistatic}}$ considers the additional range shift of point target positions from the mid-range sample as described by [26] for stripmap mode; for the TOPS mode the mid-range time of the related sub-swath is used.

$$\delta t_{az}^{\text{bistatic}} = \frac{t_{rn}^{\text{point-target}} - t_{rn}^{\text{mid-swath}}}{2}. \tag{4}$$

Figure 15 illustrates the azimuth offsets derived from each S1C measurement over the acquisition period across all Sentinel-1 modes (blue: Stripmap [SM], red: Interferometric Wide [IW], green: Extra Wide [EW]), using restituted orbit data. The offsets range between –0.6 m and +1.0 m, with a mean value of –0.15 m across all modes (**Table V**). The variability of the azimuth offset is mode dependent: higher standard deviations are observed for EW mode due to its coarser resolution, while IW mode exhibits moderate variation. For the high-resolution SM mode, the standard deviation is less than 10 cm. Overall, the residual uncertainty remains within $\pm$1.0 m for all modes, indicating that pixel positioning in azimuth remains well within the sub-pixel domain and satisfies the Sentinel-1 mission's product definition.

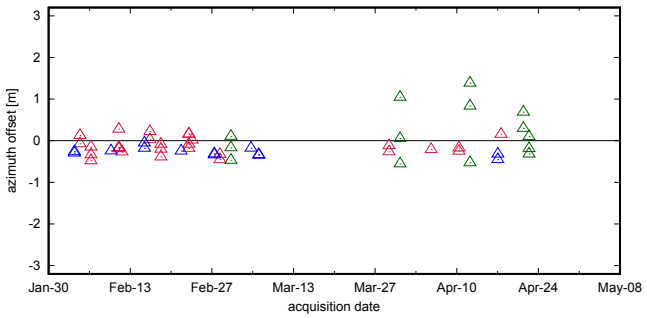

Fig. 15. Azimuth offset for all acquired overpasses derived from corner reflectors for stripmap (blue), IW (red) and EW mode (green).

B. Pixel Localization Accuracy in Range

The pixel localization accuracy in range is determined by comparing the SAR-measured round-trip signal time to a deployed target (in the Zero-Doppler plane) with the value predicted from geometry. For slant-range geometry the resulting range offset Δy (1 way) is determined from the range time difference Δt_{rn} (2 way) by multiplying with half of the signal propagation time.

$$\Delta y = \Delta t_{rn} \cdot \frac{c}{2}. \tag{5}$$

Sub-pixel resolution is achieved by interpolating the impulse response function (IRF) from the complex SAR image. To ensure accuracy, both the internal SAR instrument delay and propagation delays are corrected, with the latter dominated by tropospheric (hydrostatic) effects and minor ionospheric influences at C-band.

Tropospheric delays $\Delta r_{\text{tropospheric}}$ are addressed using zenith path delay (ZPD) values from EUREF products, adjusted for

the target's height h_{target} and incidence angle Θ according to [15] and [11].

$$\Delta r_{\text{tropospheric}} = \frac{\text{ZPD}}{cos\ \Theta} \cdot e^{-\frac{h_{\text{target}}}{8000m}}. \quad (6)$$

Ionospheric corrections utilize total electron content (TEC) values, also from EUREF, tailored to the incidence angle.

$$\Delta r_{\text{ionospheric}} = \frac{40.28\ m^3\ s^{-2}\ \cdot \text{TEC}}{f^2\ \cdot\ cos\ \Theta}. \quad (7)$$

For Sentinel-1, tropospheric corrections are typically around two meters, while ionospheric impacts are only a few centimeters.

After applying all relevant corrections, the residual range offset as a function of look angle is shown in **Figure 16**, with different acquisition modes indicated by color (SM: blue, IW: red, EW: green). For all acquisitions, the range offset remains below 2 m — most values are under 1 m — with an average of 0.55 m and a standard deviation of 0.41 m (see Table V).

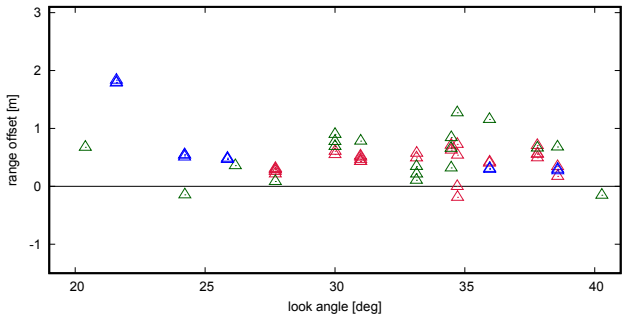

Fig. 16. Slant-range offset in dependency of look angle derived from corner reflectors for the stripmap (blue), the IW (red) and the EW-mode (green); the instrument delay and propagation effects are already corrected.

Notably, three outlier points (in blue), observed at a look angle of about 22°, have an average offset of 1.8 m. These data points correspond to Stripmap S1 beam measurements. A similar offset for the S1 beam was previously reported for S1B (but not S1A) in a geometric calibration study [11], manifesting in SLC products but disappearing when SAR processing was bypassed and raw L0 products were used. Although Sentinel-1 mission's product definition is already satisfied with the current results, further analysis of Stripmap S1C data is recommended to identify the underlying cause, which may be linked to specific auxiliary processing parameters rather than intrinsic sensor characteristics.

TABLE V
GEOMETRIC OFFSETS AND PIXEL LOCALIZATION ACCURACY IN AZIMUTH AND IN RANGE FOR DIFFERENT MODES DERIVED FROM DLR CORNER REFLECTORS.

mode	azimuth offset $\mu[m] \pm \sigma[m]$	range offset $\mu[m] \pm \sigma[m]$
SM	-0.27 ± 0.08	0.82 ± 0.61
IW	-0.14 ± 0.20	0.42 ± 0.22
EM	-0.01 ± 0.52	0.55 ± 0.27
all	-0.15 ± 0.27	0.55 ± 0.41

X. RADIOMETRIC CALIBRATION

Radiometric calibration of SAR systems is essential for converting image information from SLC products into accurate measurements of radar backscatter, such as radar cross section (RCS) or backscattering coefficients. For this process, reference targets like corner reflectors or transponders with precisely known RCS are used by analyzing the respective visible target impulse response within the SAR image. From the difference between measured RCS in a given scene and individual reference RCS of a given target, the absolute calibration factor is derived, and finally the radiometric accuracy of the whole SAR system is determined.

Our calibration concept relies on the determination of one absolute calibration factor valid for all SAR modes (Stripmap, TOPS, and WV mode) and polarization channels. Therefore, all known corrections have to be applied before estimating the calibration factor, including adjustments for the instrument's internal characteristics (see section IV), antenna beam pointing in azimuth and elevation (section VI-A and VI-B), and antenna model verification (section VII-A and VII-B). This ensures that systematic errors or gain variations across the swath and between acquisitions are minimized, regardless of orbit direction or swath position (near or far range).

Fig 17 depicts the derived absolute calibration factor for all measurements over the DLR calibration field during the S1C commissioning phase. The data points are color-coded to refer to different SAR modes: Stripmap acquisitions are marked in blue, IW in red, EW in green and WV mode in black. The different blocks visible in this plot indicate the three different observation periods:

- *Pre-CP phase* at end of January containing two EW acquisitions used for test purposes,
- *Measuring period I* from February until mid of March with a mix of SM, IW, and few EW acquisitions, and
- *Measuring period II* from mid of March until end of the CP with a mix of IW, EW, and a single S5 acquisition.

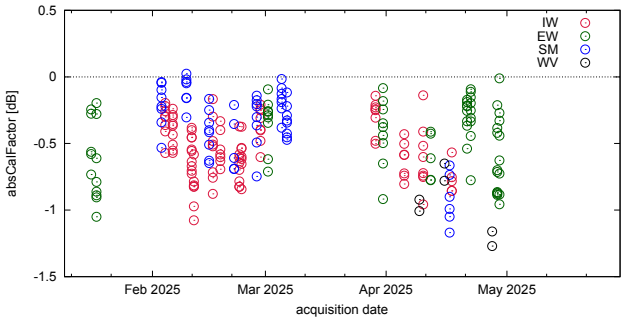

Fig. 17. Absolute calibration factor without further corrections derived from reference point targets acquired for different modes (blue: stripmap, red: IW, green: EW, black: WV).

As discussed in Section III, an orbital drift was performed by ESA at the end of March to move S1C to the nominal operation orbit. In order to consider the determined elevation pointing error (section VI-B), a permanent roll bias correction of 0.04° has been applied to the spacecraft in this transition period. This has to be considered when comparing absolute calibration factors before and after this correction by shifting

the elevation antenna pattern applied during SAR data processing accordingly.

Furthermore, a small radiometric offset was detected between absCal factors derived from TOPS SAR acquisitions (IW and EW mode) and absCal factors from Stripmap and WV mode acquisitions. It has been found that internal calibration are applied in a different way for these two groups: while for TOPS modes intermediate calibration pulses (scheduled between sub-swath switches) are frequently available and used, for Stripmap and WV mode acquisitions only pre- and postamble calibration pulses (acquired before and after SAR measurement) are taken into account. As discussed in Section IV, these offsets were estimated in a dedicated campaign, the results are summarized in Table I. According to these findings, absCal factors from Stripmap and WV mode acquisitions are corrected by 0.20 dB for co-polarized channels (HH, VV) and 0.08 dB for cross-polarized channels (HV, VH).

Finally, a too rough model approximation for calculating the observation geometry during SAR data processing has been detected by the ESA team in the middle of the commissioning phase. The geocentric Earth model used so far instead of a more accurate geodetic model introduces a latitude dependent offset which might be interpreted as an additional, but virtual, roll offset most pronounced at the poles and vanishing at the Earth equator. As a consequence the elevation antenna pattern (EAP) is not applied accurately enough due to a bias between expected and applied antenna look angle. In order to consider this radiometric bias individually, the radiometric correction has been calculated for the used point targets where the exact location is known. The EAP gain was reverted for the antenna elevation angle at the target position used during SAR data processing and re-applied for the new calculated antenna elevation angle. Note, the method for exchanging EAP and processing gain for data post-correction is described in [12].

After all corrections have been applied, radiometric calibration typically proceeds in two stages. First, relative radiometric accuracy is checked using reference targets to verify correction for any drift or antenna pattern effects within a scene. Finally, the absolute radiometric accuracy is ensured by determining the calibration factor from each target measurement and integrating results across multiple acquisitions and geometries.

A. Relative Radiometric Accuracy

For verifying the relative radiometric accuracy, the absolute calibration factor is derived from each point target deployed within the swath and compared within the acquired product. As the six available targets of the DLR calibration field aren't all simultaneously covered by each single SAR acquisition, only a limited number of measuring points is available for a given scene. Nevertheless, the variation of the derived different calibration factors from the different targets of the same SAR acquisition can be used as a measure for the relative radiometric accuracy. Note, that only co-polarized SAR data products have been chosen, so that neither acquisition mode nor polarization channel is mixed for the evaluation of a single scene.

As depicted in **Figure 18** the standard deviation derived for each scene varies between 0.03 and 0.3 dB with an average of 0.14 dB covering all 30 acquisitions with three or more data points. Neither a dependency of the acquisition mode nor of the number of covered targets is observed within the results. Both are depicted for each acquisition: the mode by color (blue: SM, red: IW, green: EW) and the number of covered targets inside the circle center.

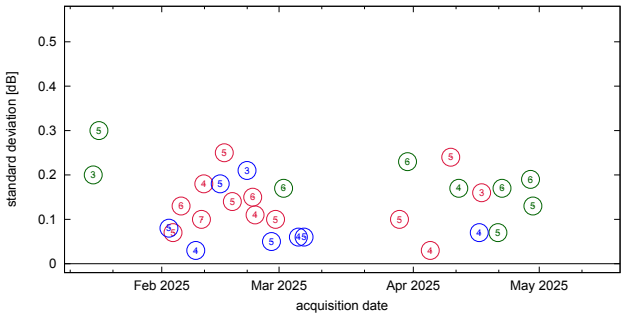

Fig. 18. Standard deviation of the calibration factor of all targets within the acquired scene evaluating co-polarization channels of related SAR products with different modes (blue: SM, red: IW, green: EW). Note, the number of covered targets within the acquisition is denoted in the circle center.

B. Absolute Radiometric Calibration

In line with the Sentinel-1 calibration strategy, a single absolute calibration factor valid across all sensor modes, beams, and subswaths has been determined. At the same time, any residual discrepancies or systematic trends between acquisition modes and polarization channels have been investigated.

From the dataset shown in **Figure 17**, the absolute calibration factor for S1C is estimated to be -0.49 dB on average with a standard deviation of 0.29 dB. The separation of results by SAR acquisition mode and polarization channel is presented in **Tables VI** and **VII**, respectively.

Furthermore, **Figure 19** illustrates the variation of the absolute calibration factor as a function of look angle, highlighting potential dependencies on antenna elevation patterns. Table VI indicates that the Stripmap, IW, and EW modes differ only slightly, with offsets on the order of 0.1–0.2 dB, each group showing a standard deviation below 0.25 dB. In contrast, WV mode exhibits larger offsets and greater variability, although only five data points are available for this configuration.

Finally, Table VII shows minor differences between polarization channels. On average, channels with horizontal transmit polarization (HH, HV) yield a slightly higher absolute calibration factor (about 0.2 dB) compared with channels transmitting vertically (VV, VH).

TABLE VI
MEAN VALUE AND STANDARD DEVIATION OF THE ABSOLUTE CALIBRATION FACTOR SEPARATING DIFFERENT SAR MODES.

SAR Mode	absolute calibration factor $\mu[dB] \pm \sigma[dB]$
SM	-0.34 ± 0.25
IW	-0.54 ± 0.21
EW	-0.46 ± 0.24
WV	-1.23 ± 0.43
all	**-0.49 ± 0.29**

TABLE VII
MEAN VALUE AND STANDARD DEVIATION OF THE ABSOLUTE CALIBRATION FACTOR SEPARATING DIFFERENT POLARIZATION CHANNELS.

Polarization Channel	absolute calibration factor $\mu[dB] \pm \sigma[dB]$
HH	-0.40 ± 0.23
HV	-0.38 ± 0.19
VV	-0.66 ± 0.35
VH	-0.67 ± 0.22

In order to derive the overall absolute radiometric accuracy of a spaceborne SAR system during the mission time, the following additional error contributions (all 1σ) have to be considered:

- a reference target accuracy of 0.2 dB,
- a dynamic range error of 0.067 dB, and
- a long term stability of the SAR instrument of 0.05 dB.

Considering all these contributions, we obtain an absolute radiometric accuracy of 0.36 dB (1σ) for S1C based on the data analyzed so far and after applying the above mentioned corrections. With additional balancing across acquisition modes and polarization channels planned in the coming months, it is expected that S1C will meet the mission requirement of an absolute radiometric accuracy better than 1 dB (3σ).

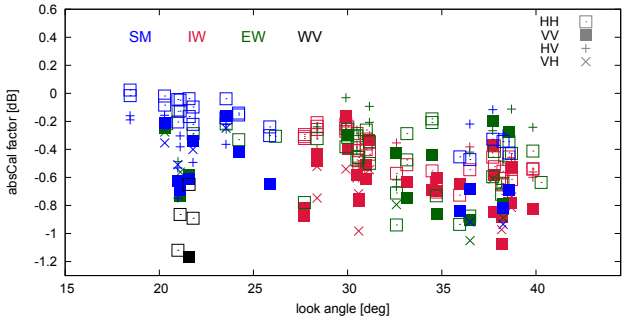

Fig. 19. Absolute calibration factor as a function of look angle, separating different polarization channels (HH, HV, VV, VH) and different SAR modes acquired (Stripmap: blue, IW: red, EW: green, WV: black).

XI. POLARIMETRIC CALIBRATION

Although Sentinel-1 is designed to transmit only a single polarization signal (either H or V), the SAR instrument is equipped with two independent receive channels, allowing both polarization components of the backscattered signal to be recorded simultaneously. This enables the generation of dual-polarization products in Stripmap, IW, and EW modes. Since WV mode provides only single-polarization products, it is excluded from the polarimetric assessment.

For these evaluations, the DLR transponders were configured with a polarization orientation of 45°. This setup ensures that the signal transmitted by the satellite (in either H or V polarization) is re-radiated by the transponder simultaneously in both H and V polarizations. From the resulting co- and cross-polarized SAR images, the channel imbalance can therefore be determined.

It should be noted that, whereas the polarization-dependent results presented in the previous section were derived as averages over all acquisitions for a given polarization channel, the results discussed here are based on dual-polarization measurements from individual acquisitions.

A. Channel Imbalance

The amplitude imbalance is specified as the ratio of the signal power in the cross-polarized channel to that of the co-polarized channel. **Figure 20** illustrates the channel imbalance as a function of look angle for the different acquisition modes: Stripmap (blue), IW (red), and EW (green).

The polarization channel combinations are distinguished by the following symbols: open squares represent dual-H polarization with horizontal transmit (HH/HV), while filled squares denote dual-V polarization with vertical transmit (VV/VH). The corresponding mean values and standard deviations are provided in **Table VIII**, separated into dual-H and dual-V polarization pairs.

The observed amplitude imbalance ranges from -0.5 dB and 0.7 dB, as shown in Figure 20. In general, dual-H polarization measurements exhibit lower mean values but larger variability compared with dual-V polarization imbalances (see Table VIII).

TABLE VIII
MEAN VALUE AND STANDARD DEVIATION OF THE CHANNEL IMBALANCE SEPARATING DIFFERENT POLARIZATION CHANNEL COMBINATIONS.

Polarization Channel	Channel imbalance $\mu[dB] \pm \sigma[dB]$
HH / HV	0.04 ± 0.24
VV / VH	0.14 ± 0.15

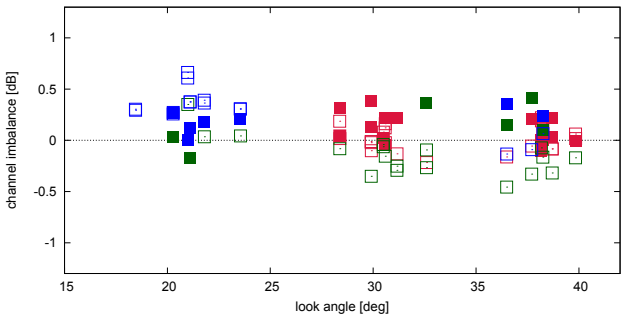

Fig. 20. Channel imbalance between cross- and co-polar channel derived from the transponder IRF for H- (open squares HH-HV in dB) and V-polarization (filled squares VV-VH in dB) on transmit for different modes (blue: SM, red: IW, green: EW).

B. Cross Talk

Cross-talk is evaluated by comparing the impulse response function of a corner reflector as derived from both polarization channels. The results obtained from all acquisitions across different modes using the DLR corner reflectors are presented in **Figure 21**. Averaging over all modes, the cross-talk remains below -40 dB confirming the excellent separation

quality between co- and cross-polarization channels in the SAR instrument's receive path.

For Stripmap (blue) and IW mode (red), cross-talk levels are consistently below -30 dB. In the case of EW mode (green), which operates at a coarser spatial resolution, slightly higher values appear for some cases, as shown in Figure 21. The reduced geometric resolution of the EW mode results in increased clutter in the cross-polarized channels, leading to greater variability and limiting the ability to verify such low cross-talk levels. Nevertheless, the results confirm the very good performance of the SAR instrument in terms of polarization channel separation for the receive path.

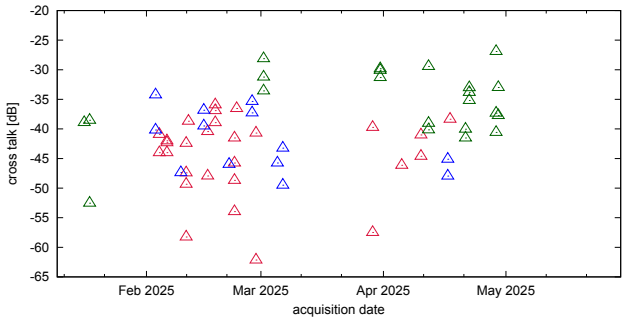

Fig. 21. Cross-talk derived from DLR corner reflectors for different modes (blue: stripmap, red: IW, green: EW).

XII. IRF BASED EVALUATIONS

In order to quantitatively assess and ensure the SAR image product quality several parameters have been evaluated from the impulse response function (IRF) of reference point targets, in particular the spatial resolution in slant range and azimuth direction, the Integrated Sidelobe Ratio (ISLR) and the Peak-to-Sidelobe Ratio (PSLR). These parameters are generally considered for quantifying the impulse response characteristics of SAR images and can be compared with the reference values from the Sentinel-1 product definition [25].

From the spatial resolution, the minimum distance is determined at which two distinct objects can be separated in the image, directly reflecting the system's ability to resolve details. For both slant range and azimuth direction, the spatial resolution is defined as the distance between the -3 dB points on the main lobe of the 1-D plots [27].

Table IX shows the estimated values for azimuth and slant range resolution derived from DLR reference point targets considering all different subswaths for IW and EW mode as well as acquired Stripmap beams S1, S2 and S5. Most of the derived resolution values match quite well with their respective product definition. There are only two exceptions found for the azimuth resolution for S1 and S5 which show higher offsets (marked by *). Analyzing this issue reveals that the currently available product definition documentation [25] doesn't reflect the values actually used by the Instrument Processing Facilities (IPF) for these beams which were changed after S1B IOC to reach similar azimuth resolution for all Stripmap beams. An updated version of the product definition will adapt the azimuth resolution of all Stripmap beams to similar values of about 4.8 - 4.9 m as measured with the DLR targets.

TABLE IX
DERIVED SPATIAL RESOLUTION FROM TARGETS' IRF WITH MEAN VALUE AND STANDARD DEVIATION FOR AZIMUTH AND SLANT RANGE DIRECTION. NOTE, THAT MARKED* VALUES WILL BE UPDATED IN THE NEXT VERSION OF THE PRODUCT DEFINITION DOCUMENTATION [25].

Mode / Beam	azimuth resolution $\mu[m] \pm \sigma[m]$	product definition (azimuth)	slant-range resolution $\mu[m] \pm \sigma[m]$	product definition (range)
S1	4.92 $\pm$ 0.01	4.3*	1.74 $\pm$ 0.01	1.7
S2	4.85 $\pm$ 0.01	4.9	2.04 $\pm$ 0.02	2.0
S5	4.82 $\pm$ 0.02	3.9*	3.36 $\pm$ 0.01	3.3
IW1	21.7 $\pm$ 0.1	21.7	2.68 $\pm$ 0.01	2.7
IW2	21.8 $\pm$ 0.1	21.7	3.12 $\pm$ 0.02	3.1
IW3	21.7 $\pm$ 0.1	21.6	3.53 $\pm$ 0.01	3.5
EW1	42.0 $\pm$ 0.2	42.2	7.94 $\pm$ 0.04	7.9
EW2	43.6 $\pm$ 0.6	42.8	10.0 $\pm$ 0.1	9.9
EW3	44.2 $\pm$ 0.5	43.6	11.8 $\pm$ 0.1	11.6
EW4	45.0 $\pm$ 0.5	44.1	13.5 $\pm$ 0.1	13.3
EW5	43.3 $\pm$ 0.5	42.6	14.6 $\pm$ 0.1	14.4

PSLR and ISLR quantify sidelobe energy relative to the main signal, reflecting sidelobe suppression and its impact on image quality and target detection. PSLR is defined as the ratio of the highest sidelobe to the main peak, while ISLR is the ratio of total sidelobe energy to main-lobe energy [27].

Figure 22 shows the derived ISLR (left) and PSLR (right) from the DLR reference point target responses acquired during S1C IOC. While the x-axis refers to the range dimension, the y-axis depicts the azimuth direction. The horizontal and vertical lines in both sub-plots mark the expected values listed in the product definition documentation [25] which is -16.1 dB for ISLR and -21.2 dB for PSLR.

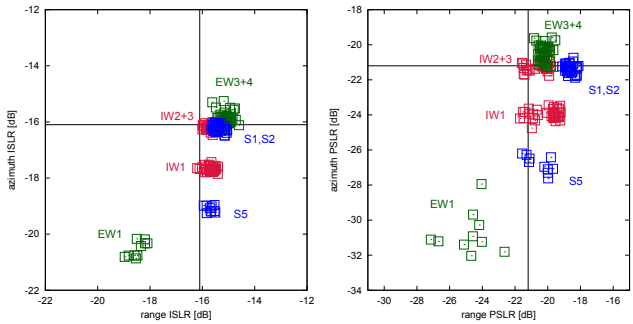

Fig. 22. ISLR (left) and PSLR (right) for range (x-axis) and azimuth (y-axis) direction derived from DLR transponder responses for different modes (blue: stripmap, red: IW, green: EW).

The derived sidelobe ratios are color coded depicting Stripmap mode in blue, IW in red and EW mode in green. A clustering behavior is visible in Fig 22 which is related to the different sub-swathes or Stripmap modes e.g. separating EW1 from EW3/4, IW1 from IW2/3 and S5 from S1/S2. In particular for the azimuth direction most of the values are near or below the product definition for both ISLR and PSLR. For the range direction a number of data points are above the product definitions as they are located on the right of the vertical line. After changing the SAR procedure (by using the measured chirp instead of nominal replica for range compression) the results are improved in particular for PSLR:

these S5 and IW acquisitions show range PSLR along the vertical line.

XIII. Sentinel-1C interferometric performance

Interferometric Synthetic Aperture Radar (InSAR) processing, based on the Terrain Observation with Progressive Scans (TOPS) acquisition mode [28], has become a cornerstone for wide area interferometric applications with the Sentinel-1 satellites. TOPS enables the acquisition of large swaths with consistently high interferometric quality. However, the TOPS acquisition mode introduces additional processing requirements when compared to the conventional stripmap acquisition mode, especially in the interferometric chain. The continuous variation of the Doppler centroid along the azimuth dimension within each burst means that misregistrations in the order of a few centimeters between the primary and secondary images can lead to azimuth-dependent phase ramps, resulting in phase discontinuities at burst edges. These artifacts might degrade the quality of the interferogram significantly, so high-precision coregistration is essential to maintain the phase quality [29], [30]. A key technique developed to overcome these challenges is Enhanced Spectral Diversity (ESD) [29], a well-established method that has been routinely used in operational InSAR processors for Sentinel-1 data for over a decade. ESD exploits the overlap regions between bursts to estimate and correct the residual azimuth misregistration with high accuracy. The results presented here are obtained using ESD within the experimental TanDEM-X Interferometric Processor (TAXI) developed at the Microwaves and Radar Institute of DLR [31]. As part of the commissioning phase of Sentinel-1C, the interferometric capabilities of the new satellite were evaluated. The interferometric investigations that have been performed in the frame of this activity are the following:

- Interferometric baseline stability: Verification of Sentinel-1's precise orbital control in order to have an orbital tube resulting in perpendicular baselines of around 120 m radius. A smaller orbital tube minimizes volume and range spectral decorrelation. Perpendicular baseline has been computed according to [32].
- Doppler common bandwidth: The spectral overlap in azimuth between primary and secondary scenes determines the usable portion of the signal. A reduced common bandwidth leads to decorrelation and, after filtering the non-common part, to a lower spatial azimuth resolution in the interferogram. The Doppler common bandwidth in TOPS is computed as follows [30]:

$$B = B_{az} - \left| \alpha \left(f_{DC,\text{pri}} - \hat{f}_{DC,\text{sec}} \right) + K_{t,\text{pri}} \cdot t_{mis} \right|, \tag{8}$$

  where B_{az} is the nominal azimuth processing bandwidth, and $|\cdot|$ is the absolute value operator. α is the TOPS scaling factor to measure the effective Doppler centroid difference. This term takes into account the electronic antenna steering and is obtained by dividing the primary Doppler rate on ground ($K_{t,\text{pri}}$) at mid-burst from the Doppler rate due to the antenna steering ($K_{s,\text{pri}}$). $f_{DC,\text{pri}}$ is the Doppler centroid of the primary acquisition at mid-burst, and $\hat{f}_{DC,\text{sec}}$ is the Doppler centroid of the of the secondary acquisition interpolated into the primary grid at mid-burst. t_{mis} is the burst mis-synchronization described in the following. According to the requirements, the common Doppler bandwidth should be larger than 95% of the nominal processing bandwidth.
- Doppler centroid stability: According to the requirements, this parameter should be on average around 0 Hzand is computed as the difference between the primary and secondary Doppler centroid for each burst.
- Burst mis-synchronization: Accurate synchronization between corresponding bursts ensures sufficient azimuth spectral overlap between bursts. The burst mis-synchronization is measured as follows [30]:

$$t_{mis} = -\left[\text{mean}\left(\Delta_{az}\right) \cdot \delta t - \left(\Delta t_{zd,\text{pri}} - \Delta t_{zd,\text{sec}}\right) \right], \tag{9}$$

  where $\text{mean}\left(\Delta_{az}\right)$ is the mean value of the azimuth offset matrix, at mid-burst; this term considers the coarse geometric coregistration error. δt is the image sampling in seconds which corresponds to about 2 msec for IW TOPS mode; $\Delta t_{zd,\text{pri}}$ and $\Delta t_{zd,\text{sec}}$ are, respectively, the primary and secondary zero Doppler shifts, each one measured as the difference between image burst start times and the sensing burst start times reported in the annotation files of Sentinel-1. According to the system requirements, the burst mis-synchronization of any single-image should not exceed ± 5 msec, which corresponds to an effective differential time shift of about ± 7 msec for an interferometric pair.

The first opportunity to evaluate the interferometric performance of Sentinel-1C was with Sentinel-1A. It is worth mentioning that, since April 2024, the Sentinel-1A satellite has an increasing orbital tube diameter due to an anomaly in a thruster. This translated in perpendicular baselines of some hundreds of meters between the two satellites. Moreover, as introduced in section III, Sentinel-1C was operated in a 1-day repeat orbit configuration w.r.t. Sentinel-1A during the first weeks of the commissioning phase. A 1-day repeat cycle significantly improves Earth observation by providing high temporal resolution, enabling near real-time monitoring of fast dynamic events such as glaciers, landslides, flooding events and particular geophysical phenomena, e.g., volcanoes and dyke intrusions. It improves interferometric consistency, especially in areas with rapid surface changes, enabling more accurate analysis of ground deformation. Frequent acquisitions support dense time series for InSAR applications and provide increased reliability through redundancy. This daily coverage also increases change detection capabilities and emergency response efforts. Overall, it enables consistent, global-scale monitoring for both scientific and operational needs. Therefore, this acquisition opportunity represented a unique chance to evaluate the benefit of such a constellation.

After the 1-day phase, a second phase was foreseen to bring the two satellites to the nominal 6-day repeat cycle. In addition, Sentinel-1C acquired data with its own 12-day repeat

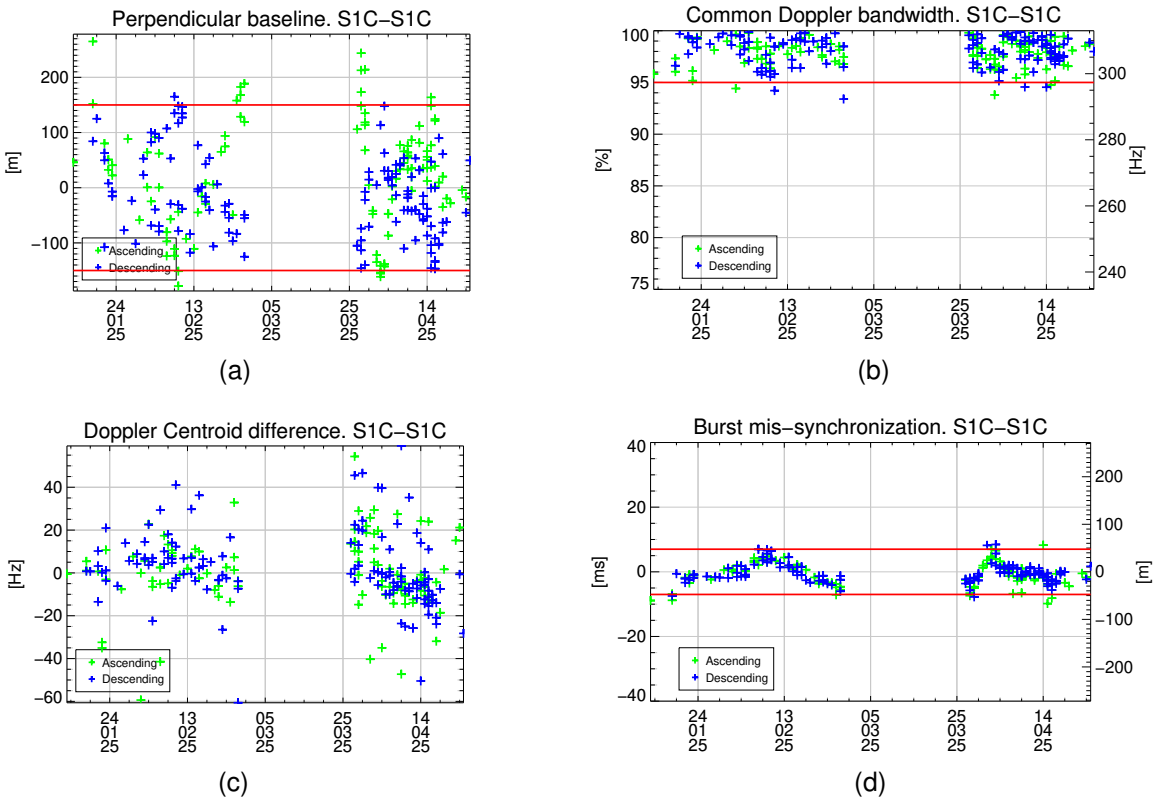

Fig. 23. Temporal analysis of the four InSAR performance parameters S1C-S1C: (a) perpendicular baseline, (b) common Doppler bandwidth, (c) Doppler Centroid difference, and (d) burst mis-synchronization. Green and blue crosses indicate, respectively, ascending and descending interferometric pairs during the first weeks of the commissioning phase

cycle allowing to generate and evaluate first Sentinel-1C co-sensor interferograms.

To describe the interferometric verification of Sentinel-1C, the sensor performance in terms of the above mentioned parameters are reported first, showing the excellent Sentinel-1C performance, which is a prerequisite for TOPS interferogram generation. Then, a section is dedicated to report the interferometric results of the first Sentinel-1C interferograms, both cross-sensor and co-sensor, including acquisition over non-stationary scenarios.

A. Sentinel-1C InSAR performance

The performance evaluation of Sentinel-1C comprises two complementary analyses: Monitoring the global performance of the satellite and examining long data acquisitions for degradation of the InSAR parameters. This section mainly presents the results by evaluating co-sensor interferograms, i.e., based on pairs of Sentinel-1C acquisitions, which provide insights into the stability and reliability of Sentinel-1C operations.

1) Statistical analysis of main InSAR parameters: In the co-sensor analysis, the mentioned key performance parameters are analyzed: Perpendicular baseline, common Doppler bandwidth, Doppler centroid difference and burst mis-synchronization. The results show that Sentinel-1C performs exceptionally well in co-sensor mode. All parameters fulfill or exceed the respective requirements. In particular, an exhaustive analysis of 134 Sentinel-1C/Sentinel-1C pairs have been conducted during the commissioning phase. Results are shown in **Figure 23**:

A stable vertical baseline distribution, reported in **Figure 23a**, mostly within the range of ± 120 meters could be observed, confirming the very good orbit control. Concerning the Doppler common bandwidth, summarized in **Figure 23b**, the result of the analysis related to the evaluated InSAR pairs confirmed the outstanding Sentinel-1C performance with the minimum requirement of nominal common Doppler bandwidth of 95% largely exceeded. The stability of the Doppler centroid difference is also confirmed with a retrieved -7 Hz averaged value of such parameter (see **Figure 23c**). Finally, evaluating the burst mis-synchronization, Sentinel-1C exhibits an excellent alignment among bursts, as reported in **Figure 23d** with all values well within the acceptable range of ± 7 milliseconds.

As one can observe, there is a gap in the measurements for the month of March. During this period, Sentinel-1C underwent a critical maneuver to be repositioned into its nominal orbit with a 6-day repeat w.r.t. Sentinel-1A. The graphs also show that Sentinel-1C performance remains excellent after repositioning and in line with those obtained before the orbit maneuver.

For completeness, **Table X** reports the mean and standard deviation of the considered Sentinel-1C InSAR performance parameters. Note that the standard deviation of the burst mis-synchronization has been divided by $\sqrt{2}$ to compare it to the

TABLE X
CO-SENSOR TOPS INSAR METRICS SUMMARY

Metrics	Mean	Standard Deviation
Perpendicular Baseline [m]	71.1	51.4
Common Doppler Bandwidth [Hz]	306.7	4.2
Doppler Centroid Difference [Hz]	0.4	17.1
Burst Mis-synchronization [ms]	-0.6	2.3

single-image requirement of 5 milliseconds.

As mentioned above, the first opportunity to generate an interferogram using Sentinel-1C involved combining its data with those of Sentinel-1A, i.e., to generate a cross-platform interferogram. For this purpose, the same cross-sensor performance analysis was conducted. The baseline distribution was stable, despite the large absolute values caused by Sentinel-1A's relatively loose orbit control. This parameter also contributed to sub-optimal Doppler and burst mis-synchronisation performance. Although the latter slightly exceeded the specified requirements, it remained more than sufficient to produce high-quality interferograms, as demonstrated in the following section XIII-B.

2) Long data take analysis: To evaluate the stability of Sentinel-1C's InSAR performance over extended time intervals, the previous interferometric evaluations were performed on long data takes. The analyses was done for both ascending and descending acquisition with a duration of at least 6 minutes. The results show that Sentinel-1C consistently meet the required InSAR performance criteria also for such configurations. The common Doppler bandwidth remained above 95% of the nominal value in all subswaths and datasets. The baseline analysis confirms that the satellite operated within the nominal tube for both ascending and descending orbits. Furthermore, the burst mis-synchronization remained below 2.5 ms, comfortably satisfying the 7 ms requirement. These results confirm Sentinel-1C's stability and reliability for long acquisitions.

B. Sentinel-1C Interferometric Results

This section presents the interferometric results of Sentinel-1C obtained during the commissioning phase. The first interferograms generated using both cross-sensor and co-sensor data are introduced, in both cases with acquisitions over the Atacama Desert region.

Sentinel-1C's interferometric capabilities are further validated through an analysis on the Zachariæ Isstrøm Glacier, a challenging non-stationary environment. This region exemplifies how the satellite can handle dynamic scenarios, where the 1-day repeat cycle can be fully exploited to monitor rapid surface changes. The results confirm that Sentinel-1C meets the technical requirements for InSAR applications, even under complex and changing conditions. Overall, the analysis underlines the satellite's robustness and reliability in generating interferograms, both in stable and dynamic contexts. These results highlight its potential for a wide range of Earth observation tasks, from seismic monitoring to glacial dynamics, and solidify its role as a key asset in the Sentinel-1 constellation.

1) First Sentinel-1C interferograms: Atacama Desert: The Atacama Desert is used as a SAR test site due to its extremely dry climate, sparse vegetation and stable surface conditions. These characteristics ensure coherent backscatter and minimal temporal decorrelation, ideal for the calibration and validation of space radar systems.

The left column of **Figure 24** provides the first cross-sensor Sentinel-1C/Sentinel-1A InSAR results obtained over the Atacama test site for the 1-day repeat-pass phase [33]. The data have been acquired on 19 and 20 January 2025 in an ascending configuration with the IW mode with Sentinel-1A and Sentinel-1C, respectively. **Figure 24a** shows the scene characteristics out of the Sentinel-1C amplitude image. Considering now the interferometric processing, **Figure 24c** and **Figure 24e** present the coherence and the phase. A remarkably consistently high level of coherence in the area, with values predominantly close to unity, can be observed. Due to the relatively large perpendicular baseline (about 490 meters in this case) some coherence decorrelation can be observed, occurring mainly due to volumetric scatterers. Considering now the interferometric phase, no phase discontinuities between bursts or sub-swaths can be observed, confirming the accuracy of the complete processing chain, including image formation and interferometric processing. The phase patterns that can be observed are mainly related to atmospheric contributions, mainly atmosphere and ionosphere [34], since the DEM component was removed using the $90\,m$ TanDEM-X DEM [35].

The first Sentinel-1C co-sensor InSAR results have been obtained by combining the acquisitions that took place on 20 January 2025 and 1 February 2025. Also for this case, the acquisition was performed with the IW-mode in ascending orbit configuration [33]. The results are reported in the right column of **Figure 24**. The amplitude image of **Figure 24b** reveals subtle surface textures with no obvious artifacts, while the interferometric coherence, reported in **Figure 24d**, remains incredibly high, confirming negligible temporal, volumetric or spectral decorrelation between acquisitions. The interferometric phase, shown in **Figure 24f**, reports excellent continuity in both bursts and subswaths, further validating the accuracy of the processing chain. Similar as before, the main phase contributions are due to atmospheric signals.

2) Non-stationary scenarios: Zachariæ Isstrøm glacier: Zachariæ Isstrøm, a dynamic tidewater glacier located in north-east Greenland, plays a crucial role in understanding glacier behavior and climate change. Its rapid ice discharge and significant retreat in recent decades make it an important object of study. InSAR is used to monitor the glacier's ice flow velocity [36], surface deformation [37], [38] and retreat patterns, providing valuable information on its changing dynamics. Characterized by high-speed ice movement, reaching several kilometers per year, the Zachariæ Isstrøm has shown accelerated flow and thinning during the last decades mainly driven by ocean-induced melting and ice shelf destabilization [39].

Data acquired by Sentinel-1C and Sentinel-1A on the 5 and 6 March 2025 (at the end of the winter season) in descending orbit and IW-mode, have been processed and the resulting InSAR outcome is reported in **Figure 25**. In

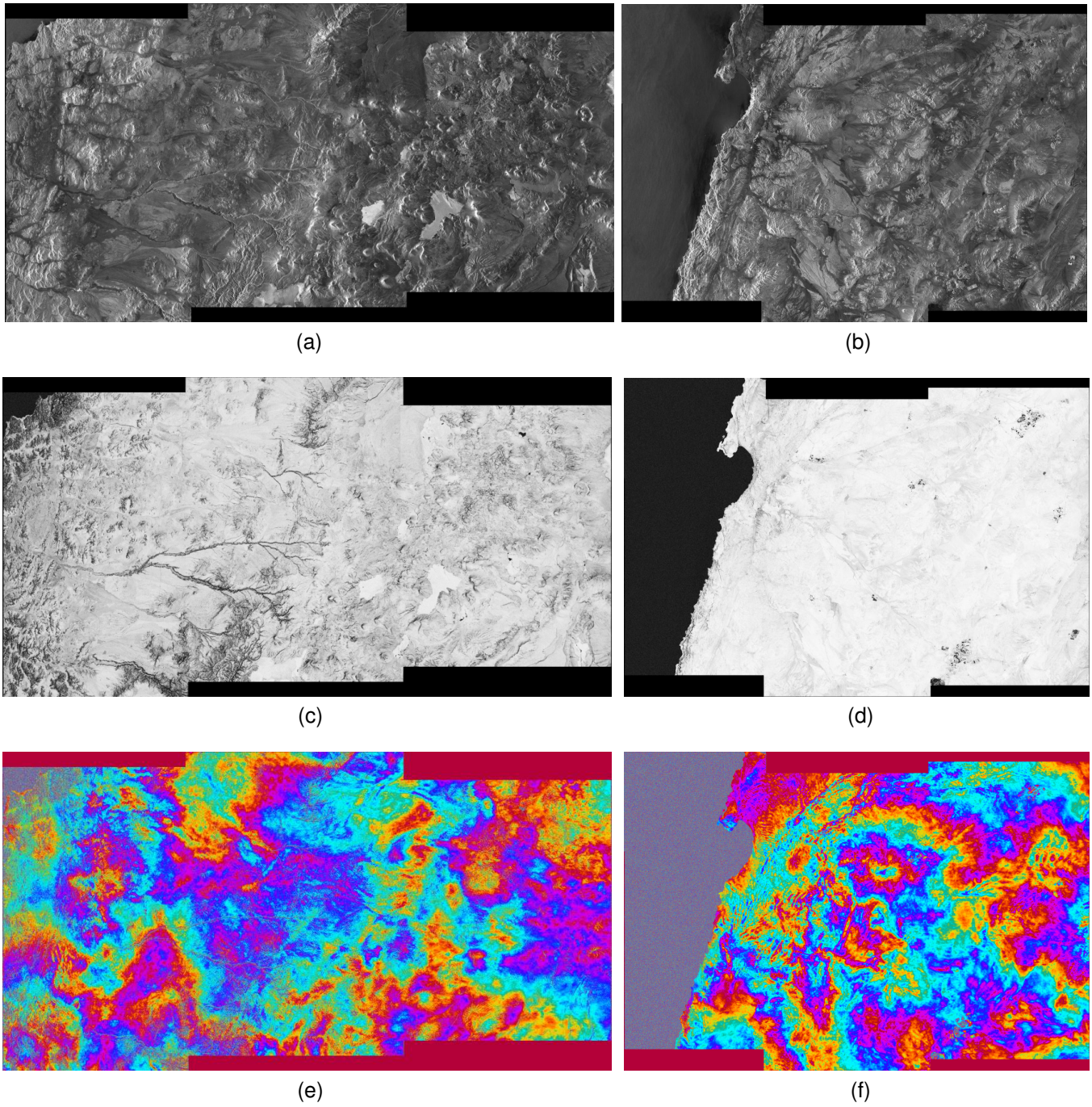

Fig. 24. Interferometric results over the Atacama desert for the cross-sensor 1-day repeat-pass (left column) and co-sensor 12-day repeat-pass (right column) configurations. Panels (a,b) show the amplitude images, (c,d) the interferometric coherence, and (e,f) the topography-compensated interferometric phase.

Figure 25a the amplitude image is reported where the ice features are nicely captured. **Figure 25b** shows a coherence map mostly close to one, except for some areas on the left of the acquisition, where the coherence drops to zero due to the motion of floating ice. The presence of phase discontinuities in the flattened interferometric phase depicted in **Figure 25c** confirm the ground motion due to glacier flows and large-scale displacements occurring over the area. A 1-day repeat SAR cycle represents a unique chance to gather important data over areas like Zachariæ Isstrøm and allows frequent observation of rapid ice movements and changes in the glacier surface. This frequent monitoring improves data quality by reducing errors and helps track short-term changes more accurately. It also allows for the rapid detection of events such as ice calving, supporting a better understanding of glacier behavior and predictions of sea level rise.

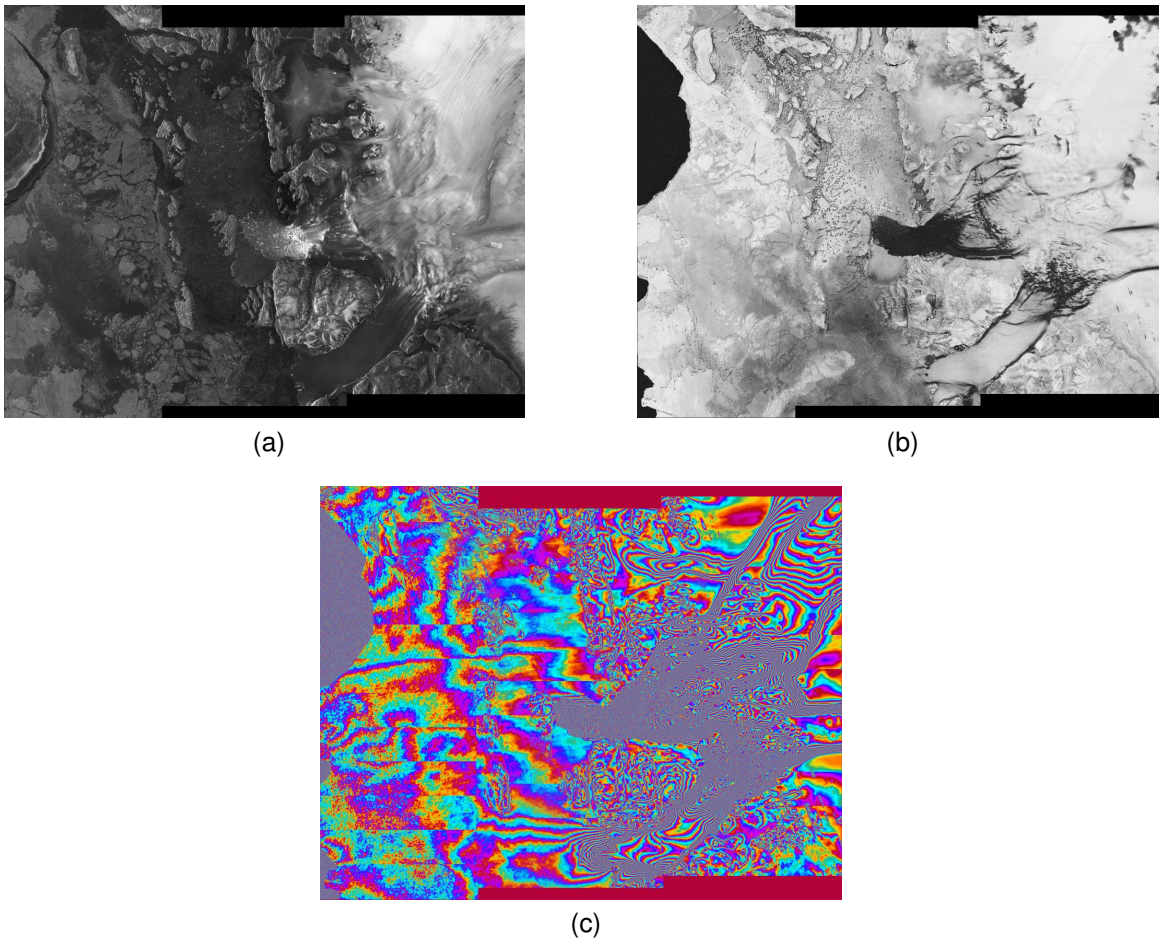

Fig. 25. Interferogram over Zachariæ Isstrøm glacier. (a) amplitude, (b) interferometric coherence and (c) topography-compensated interferometric phase.

XIV. Conclusions

In this paper, we presented the results of DLR's independent SAR system calibration campaign of S1C executed successfully during the Sentinel-1C commissioning phase. In conclusion, we find that S1C achieves or even exceeds all SAR performance requirements put forth and is ready for its nominal mission operations. At the end of the commissioning phase, the SAR instrument is in good health. The implemented hardware improvements of S1C over the previous two S1 units have resulted in a clear improvement of the SAR performance, most directly visible in the improved sensitivity. We demonstrated an excellent interferometric performance which became evident already early on in the commissioning phase.

Provided the second unit of this generation, S1D, shows similar performance, the Sentinel-1 constellation will be well-equipped for supporting its multitude of operational Earth observation objectives and applications for the foreseeable future.

Acknowledgements

The results presented here are partially outcome of the ESA contract No. 4000136585/21/NL/NA Sentinel-1C Independent In-Orbit Calibration. The Copernicus Sentinel-1 mission is funded by the EU and ESA. The views expressed herein can in no way be taken to reflect the official opinion of the European Space Agency or the European Union.

Program of the European Union implemented by esa

REFERENCES

[1] R. Torres, P. Snoeij, D. Geudtner, D. Bibby, M. Davidson, E. Attema, P. Potin, B. Rommen, N. Floury, M. Brown, I. N. Traver, P. Deghaye, B. Duesmann, B. Rosich, N. Miranda, C. Bruno, M. L'Abbate, R. Croci, A. Pietropaolo, M. Huchler, and F. Rostan, "GMES Sentinel-1 mission," *Remote Sensing of Environment*, vol. 120, pp. 9–24, 2012. [Online]. Available: https://doi.org/10.1016/j.rse.2011.05.028

[2] R. Torres, I. Navas-Traver, D. Bibby, S. Lokas, P. Snoeij, B. Rommen, S. Osborne, F. Ceba-Vega, P. Potin, and D. Geudtner, "Sentinel-1 SAR System and Mission," in *2017 IEEE Radar Conference (RadarConf)*, May 2017, pp. 1582–1585. [Online]. Available: https://ieeexplore.ieee.org/abstract/document/7944460

[3] R. Torres, D. Geudtner, S. Lokas, D. Bibby, P. Snoeij, I. N. Traver, F. Ceba Vega, J. Poupaert, and S. Osborne, "Sentinel-1 Satellite Evolution," in *IGARSS 2018 - 2018 IEEE International Geoscience and Remote Sensing Symposium*, July 2018, pp. 1555–1558. [Online]. Available: https://ieeexplore.ieee.org/abstract/document/8517899

[4] R. Torres, S. Lokas, G. Di Cosimo, D. Geudtner, and D. Bibby, "Sentinel 1 Evolution: Sentinel-1C and -1D Models," in *2017 IEEE International Geoscience and Remote Sensing Symposium (IGARSS)*, July 2017, pp. 5549–5550. [Online]. Available: https://ieeexplore.ieee.org/abstract/document/8128261

[5] P. Klenk, J. Giez, K. Schmidt, M. Nannini, and M. Schwerdt, "Independent Calibration of the Sentinel-1C SAR System," in *EUSAR 2024; 15th European Conference on Synthetic Aperture Radar*, April 2024, pp. 591–594. [Online]. Available: https://ieeexplore.ieee.org/abstract/document/10659593

[6] J. Reimann, M. Schwerdt, K. Schmidt, N. T. Ramon, and B. Döring, "The DLR Spaceborne SAR Calibration Center," *Frequenz*, vol. 71, no. 11-12, pp. 619–627, 2017. [Online]. Available: https://doi.org/10.1515/freq-2016-0274

[7] M. Schwerdt, B. Doring, M. Zink, B. Brautigam, and D. Schrank, "Innovative and efficient strategy of calibrating Sentinel-1," in *2009 IEEE International Geoscience and Remote Sensing Symposium*, vol. 1, July 2009, pp. I–48–I–51. [Online]. Available: https://ieeexplore.ieee.org/abstract/document/5416945

[8] M. Schwerdt, B. Döring, M. Zink, and D. Schrank, "In-Orbit Calibration Plan of Sentinel-1," in *8th European Conference on Synthetic Aperture Radar*, June 2010, pp. 350–352. [Online]. Available: https://ieeexplore.ieee.org/abstract/document/5758738

[9] M. Jirousek, B. Doering, D. Rudolf, S. Raab, and M. Schwerdt, "Development of the highly accurate DLR Kalibri Transponder," in *EUSAR 2014; 10th European Conference on Synthetic Aperture Radar*, June 2014, pp. 1176–1179. [Online]. Available: https://ieeexplore.ieee.org/abstract/document/6857011

[10] B. J. Döring, J. Reimann, S. Raab, M. Jirousek, D. Rudolf, and M. Schwerdt, "The Three-Transponder Method: A Novel Method for Accurate Transponder RCS Calibration," *Progress In Electromagnetics Research B*, vol. 61, pp. 297–315, 2014. [Online]. Available: http://dx.doi.org/10.2528/PIERB14110406

[11] K. Schmidt, J. Reimann, N. Tous Ramon, and M. Schwerdt, "Geometric Accuracy of Sentinel-1A and 1B Derived from SAR Raw Data with GPS Surveyed Corner Reflector Positions," *Remote Sensing*, vol. 10, no. 4: 523, 2018. [Online]. Available: https://www.mdpi.com/2072-4292/10/4/523

[12] K. Schmidt, M. Schwerdt, G. Hajduch, P. Vincent, A. Recchia, and M. Pinheiro, "Radiometric Re-Compensation of Sentinel-1 SAR Data Products for Artificial Biases due to Antenna Pattern Changes," *Remote Sensing*, vol. 15, no. 5: 1377, 2023. [Online]. Available: https://www.mdpi.com/2072-4292/15/5/1377

[13] K. Weidenhaupt, A.-M. Buechner, M. Jirousek, S. Raab, J. Reimann, and M. Schwerdt, "DLR's next generation of multi-band transponders for the calibration of fully polarimetric SAR missions," in *EUSAR 2022; 14th European Conference on Synthetic Aperture Radar*, July 2022, pp. 90–94. [Online]. Available: https://ieeexplore.ieee.org/abstract/document/9944221

[14] A. M. Büchner, K. Weidenhaupt, B. Gabler, M. Limbach, and M. Schwerdt, "Mitigation of Mutual Antenna Coupling Effects for Active Radar Targets in L-Band," *Remote Sensing*, vol. 13, no. 22: 4614, 2021. [Online]. Available: https://www.mdpi.com/2072-4292/13/22/4614

[15] M. Schwerdt, K. Schmidt, N. Tous Ramon, G. Castellanos Alfonzo, B. J. Döring, M. Zink, and P. Prats-Iraola, "Independent Verification of the Sentinel-1A System Calibration," *IEEE Journal of Selected Topics in Applied Earth Observations and Remote Sensing*, vol. 9, no. 3, pp. 994–1007, 2016. [Online]. Available: https://doi.org/10.1109/JSTARS.2015.2449239

[16] M. Schwerdt, K. Schmidt, N. Tous Ramon, G. Castellanos Alfonzo, B. Doering, M. Zink, and P. Prats, "Independent Verification of the Sentinel-1A System Calibration - First Results," in *EUSAR 2014; 10th European Conference on Synthetic Aperture Radar*, June 2014, pp. 1259–1262. [Online]. Available: https://ieeexplore.ieee.org/document/6857032

[17] M. Schwerdt, K. Schmidt, N. Tous Ramon, P. Klenk, N. Yague-Martinez, P. Prats-Iraola, M. Zink, and D. Geudtner, "Independent System Calibration of Sentinel-1B," *Remote Sensing*, vol. 9, no. 6: 511, 2017. [Online]. Available: https://www.mdpi.com/2072-4292/9/6/511

[18] K. Schmidt, M. Schwerdt, N. Miranda, and J. Reimann, "Radiometric Comparison within the Sentinel-1 SAR Constellation over a Wide Backscatter Range," *Remote Sensing*, vol. 12, no. 5, 2020. [Online]. Available: https://www.mdpi.com/2072-4292/12/5/854

[19] D. Hounam, M. Schwerdt, and M. Zink, "Active Antenna Module Characterisation by Pseudo-Noise Gating," in *25th ESA Antenna Workshop on Satellite Antenna Technology*, 2002.

[20] M. Schwerdt, N. Tous Ramon, J. Giez, and K. Schmidt, "SAR Calibration Algorithms," German Aerospace Center (DLR), Microwaves and Radar Institute, Tech. Rep. S1CD-DD-DLR-SY04-0001, 2022.

[21] H. Flachs, S. Diel, P. Kozakowski, C. Plaindoux, and M. Glatt, "SAR Instrument Calibration and Characterization Plan," Airbus Defence and Space GmbH, Tech. Rep. S1CD-PL-ASD-IN06-0013, 2024.

[22] P. Potin, M. Pinheiro, R. Torres, D. Geudtner, D. Bibby, I. Navas-Traver, M. Cossu, and S. Graham, "Sentinel-1A/-1B Mission and Performance Status, Sentinel-1C/-1D Improvements," in *EUSAR 2022; 14th European Conference on Synthetic Aperture Radar*, July 2022, pp. 141–146. [Online]. Available: https://ieeexplore.ieee.org/abstract/document/9944231

[23] E. Schied, S. Idler, I. Navas-Traver, F. C. Vega, P. Snoeij, and D. J. Bibby, "The Sentinel-1 C & D SAR Instrument," in *EUSAR 2018; 12th European Conference on Synthetic Aperture Radar*, June 2018, pp. 632–635. [Online]. Available: https://ieeexplore.ieee.org/abstract/document/8438081

[24] J. Fernández, H. Peter, C. Fernández, J. Berzosa, M. Fernández, L. Bao, M. Ángel Muñoz, S. Lara, E. Terradillos, P. Féménias, and C. Nogueira, "The Copernicus POD Service," *Advances in Space Research*, vol. 74, no. 6, pp. 2615–2648, 2024, global Navigation Satellite Systems: Recent Scientific Advances. [Online]. Available: https://www.sciencedirect.com/science/article/pii/S0273117724001984

[25] H. Laur, P. Bally, P. Meadows, J. Sanchez, B. Schaettler, E. Lopinto, and D. Esteban, "Sentinel-1 Product Definition," S1-RS-MDA-52-7440, Issue 2.7, Tech. Rep., Mar. 25/03/2016. [Online]. Available: https://sentiwiki.copernicus.eu/web/document-library#DocumentLibrary-SENTINEL-1DocumentsLibrary-S1-Documents

[26] A. Schubert, D. Small, N. Miranda, D. Geudtner, and E. Meier, "Sentinel-1A Product Geolocation Accuracy: Commissioning Phase Results," *Remote Sensing*, vol. 7, no. 7, pp. 9431–9449, 2015. [Online]. Available: https://www.mdpi.com/2072-4292/7/7/9431

[27] A. Freeman, "SAR calibration: An Overview," *IEEE Transactions on Geoscience and Remote Sensing*, vol. 30, no. 6, pp. 1107–1121, Nov 1992. [Online]. Available: https://ieeexplore.ieee.org/abstract/document/193786

[28] F. De Zan and A. Monti Guarnieri, "TOPSAR: Terrain Observation by Progressive Scans," *IEEE Transactions on Geoscience and Remote Sensing*, vol. 44, no. 9, pp. 2352–2360, 2006. [Online]. Available: https://ieeexplore.ieee.org/document/1677745

[29] P. Prats-Iraola, R. Scheiber, L. Marotti, S. Wollstadt, and A. Reigber, "TOPS Interferometry With TerraSAR-X," *IEEE Transactions on Geoscience and Remote Sensing*, vol. 50, no. 8, pp. 3179–3188, Aug. 2012. [Online]. Available: https://ieeexplore.ieee.org/document/6130599

[30] N. Yague-Martinez, P. Prats-Iraola, F. R. Gonzalez, R. Brcic, R. Shau, D. Geudtner, M. Eineder, and R. Bamler, "Interferometric processing of Sentinel-1 TOPS data," *IEEE Transactions on Geoscience and Remote Sensing*, vol. 54, no. 4, pp. 2220–2234, 2016. [Online]. Available: https://ieeexplore.ieee.org/document/7390052

[31] P. Prats-Iraola, M. Rodriguez-Cassola, L. Marotti, M. Nannini, S. Wollstadt, D. Schulze, N. Tous-Ramon, M. Younis, G. Krieger, and A. Reigber, "TAXI: A Versatile Processing Chain for Experimental TanDEM-X Product Evaluation," in *Proceedings of the IEEE Geoscience and Remote Sensing Symposium (IGARSS)*. IEEE, Juli 2010, pp. 1–4. [Online]. Available: https://elib.dlr.de/63708/

[32] E. Sansosti, "A simple and exact solution for the interferometric and stereo SAR geolocation problem," *IEEE Transactions on Geoscience*

and Remote Sensing, vol. 42, no. 8, pp. 1625–1634, 2004. [Online]. Available: https://doi.org/10.1109/TGRS.2004.831442

[33] European Space Agency, "*Sentinel-1C demonstrates power to map land deformation*," [Online]. Available: https://www.esa.int/Applications/Observing_the_Earth/Copernicus/Sentinel-1/Sentinel-1C_demonstrates_power_to_map_land_deformation, 2022.

[34] F. De Zan, P. Prats-Iraola, R. Scheiber, and A. Rucci, "Interferometry with TOPS: coregistration and azimuth shifts," in *EUSAR 2014; 10th European Conference on Synthetic Aperture Radar*, 2014, pp. 1–4. [Online]. Available: https://ieeexplore.ieee.org/document/6856955

[35] G. Krieger, M. Zink, M. Bachmann, B. Bräutigam, D. Schulze, M. Martone, P. Rizzoli, U. Steinbrecher, J. Walter Antony, F. De Zan, I. Hajnsek, K. Papathanassiou, F. Kugler, M. Rodriguez-Cassola, M. Younis, S. Baumgartner, P. López-Dekker, P. Prats-Iraola, and A. Moreira, "TanDEM-X: A radar interferometer with two formation-flying satellites," *Acta Astronautica*, vol. 89, pp. 83–98, 2013. [Online]. Available: https://doi.org/10.1016/j.actaastro.2013.03.008

[36] J. K. Andersen, A. Kusk, J. P. Merryman Boncori, C. S. Hvidberg, and A. Grinsted, "Improved Ice Velocity Measurements with Sentinel-1 TOPS Interferometry," *Remote Sensing*, vol. 12, no. 12, 2020. [Online]. Available: https://doi.org/10.3390/rs12122014

[37] R. Scheiber, M. Jäger, P. Prats-Iraola, F. De Zan, and D. Geudtner, "Speckle Tracking and Interferometric Processing of TerraSAR-X TOPS Data for Mapping Nonstationary Scenarios," *IEEE Journal of Selected Topics in Applied Earth Observations and Remote Sensing*, vol. 8, no. 4, pp. 1709–1720, 2015. [Online]. Available: https://ieeexplore.ieee.org/document/6926747

[38] R. Grandin, E. Klein, M. Métois, and C. Vigny, "Three-dimensional displacement field of the 2015 Mw8.3 Illapel earthquake (Chile) from across- and along-track Sentinel-1 TOPS interferometry," *Geophysical Research Letters*, vol. 43, no. 6, pp. 2552–2561, 2016. [Online]. Available: https://doi.org/10.1002/2016GL067954

[39] L. An, E. Rignot, M. Wood, J. Willis, J. Mouginot, and S. A. Khan, "Ocean melting of the Zachariae Isstrøm and Nioghalvfjerdsfjorden glaciers, northeast Greenland," *Proceedings of the National Academy of Sciences*, vol. 118, p. e2015483118, 01 2021. [Online]. Available: 10.1073/pnas.2015483118

Patrick Klenk is a Senior Research Scientist with the SAR Calibration Center of DLR's Microwaves and Radar Institute, Oberpfaffenhofen, Germany. He received his doctoral degree in Physics from Heidelberg University, Heidelberg, Germany, in 2012 for his dissertation on "Ground-Penetrating Radar for Quantitative Soil Hydrology." After three more years of postdoctoral work with the Heidelberg University's Institute of Environmental Physics, he joined the German Aerospace Center's Microwaves and Radar Institute in 2016.

Since then, Dr. Klenk has been developing novel SAR calibration techniques with a focus on antenna aspects for current and future satellite SAR systems such as Tandem-L, TerraSAR-X, TanDEM-X, PAZ, and ESA's Sentinel-1A/B/C/D, while also being responsible for instrument operations of the TerraSAR-X and Tandem-X missions. Since 2018, he has been heading SAR system calibration related projects for various ESA missions and mission proposals such as ROSE-L, Sentinel-1NG, LEOB and HydroTerra and most recently BIOMASS. On behalf of ESA, he is currently leading a team responsible for planning and implementing DLR's independent SAR calibration campaigns during the in-orbit commissioning of Sentinel-1C in 2025 and in 2026 the Sentinel-1D mission.

Jakob Giez received his Masters degree in electrical engineering and information theory from the Technical University of Munich in 2021 with a thesis on adaptive SAR quantization with staggered SAR. Since 2021 he has been with the German Aerospace Center (DLR) in Oberpfaffenhofen. He works as an research scientist in the Microwaves and Radar Institute with the Calibration Group for SAR satellite systems.He is responsible for the calibration support with focus on internal calibration for different SAR missions, as for ESA's Sentinel-1C/D and ROSE-L mission. His major major research interests include remote sensing, and SAR system calibration.

Kersten Schmidt received the Diploma degree in physics from University of Freiburg in 1998, the Ph.D. degree in atmospheric science from the University of Munich in 2007 with a thesis on lightning detection by analysing lightning induced electromagnetic pulses. Since 2009 he has been with German Aerospace Center (DLR) in Oberpfaffenhofen, Germany. Since 2012 he works as project engineer and scientist at Microwave and Radar Institute at DLR with the Calibration Group for SAR satellite systems. There he is responsible for the calibration support for different satellite SAR missions in the field of geometric and radiometric calibration. Currently his major research interests include electromagnetic wave propagation, remote sensing, and SAR system calibration.

Matteo Nannini received his laurea degree in Telecommunication Engineering from the University of Florence (2003), where he completed his thesis in collaboration with the Microwaves and Radar Institute of the German Aerospace Center (DLR). He later received his Ph.D. degree in Electrical Engineering from the Karlsruhe Institute of Technology, with research focused on synthetic aperture radar (SAR) tomography. Since 2004, he has been with the Microwaves and Radar Institute of DLR, working on a range of topics, including SAR processing, SAR interferometry, SAR tomography, spectral estimation techniques, radar ice sounding, and persistent scatterer interferometry time-series analysis. He contributed to the development of ground processing prototypes for upcoming ESA missions such as BIOMASS and ROSE-L, and was involved in the in-orbit commissioning phase of Sentinel-1C.

Andrea Pulella received the Laurea (M.S.) degree (summa cum laude) in Telecommunications Engineering from the University of Pisa, Pisa, Italy, in 2017. Since December 2017, he has been with the Microwaves and Radar Institute, German Aerospace Center (DLR), Weßling, Germany, as a research engineer in the area of synthetic aperture radar (SAR) remote sensing. He is currently involved in the development of the ground processor prototype for ESA's ROSE-L mission. Additionally, he supports the PRISM (Processor for Interferometric SAR Missions) software at DLR as a developer. He contributed to the in-orbit commissioning phase of Sentinel-1C and is also involved in preparations for Sentinel-1D. His research interests include SAR interferometry (InSAR), advanced interferometric acquisition modes, and end-to-end SAR simulation. Recent interests concern the development of deep learning algorithms for statistical inference in interferometric phase source separation, representation learning, land cover classification, and automatic target recognition using SAR data.

Pau Prats-Iraola (Fellow, IEEE) was born in Madrid, Spain, in 1977. He received the Ingeniero and Ph.D. degrees in telecommunications engineering from the Universitat Politècnica de Catalunya (UPC), Barcelona, Spain, in 2001 and 2006, respectively. In 2001, he was a Research Assistant with the Institute of Geomatics, Spain. In 2002, he was with the Department of Signal Theory and Communications, UPC, where he worked in the field of airborne repeat-pass interferometry and airborne differential SAR interferometry. From December 2002 to August 2006, he was an Assistant Professor with the Department of Telecommunications and Systems Engineering, Universitat Autònoma de Barcelona, Barcelona, Spain. In 2006, he joined the Microwaves and Radar Institute, German Aerospace Center (DLR), Weßling, Germany, where, since 2009, he has been the Head of the Multimodal Algorithms Group. He is the responsible and main developer of the TanDEM-X Interferometric (TAXI) processor, an end-to-end processing chain for data acquired by the TerraSAR-X and TanDEM-X satellites, which has been used to demonstrate novel SAR acquisition modes and techniques. He is currently involved in the design and implementation of the ground processor prototypes and end-to-end simulators of ESA's BIOMASS and ROSE-L missions. His research interests include high-resolution airborne/spaceborne monostatic/bistatic SAR processing, SAR interferometry, advanced interferometric acquisition modes, persistent scatterer interferometry (PSI), SAR tomography, and end-to-end SAR simulation. He has co-authored more than 60 peer-reviewed journal articles in the field.

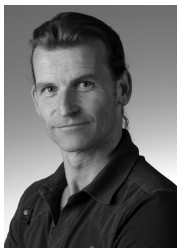

Marco Schwerdt received the Dipl.-Ing. degree in electrical engineering and the Dr.-Ing. degree with a thesis on electrooptical E-field sensors from the Technical University Berlin, Germany, 1998. Since 1998, he has been with the Microwave and Radar Institute, German Aerospace Center (DLR), Oberpfaffenhofen, Germany, where he is working on SAR calibration methods and performance analysis tools. Since 2000, he has been the Head of the Radar Calibration Group performing various radar calibration activities for different SAR missions like XSAR/SRTM or the ScanSAR mode of ASAR/Envisat. He was responsible for the successful calibration of the German TerraSAR-X and TanDEM-X satellites, launched in 2007 and 2010, respectively. Furthermore, in the frame of ESA's Sentinel-1 SAR mission as part of the Copernicus program, he was responsible for developing the overall SAR system calibration and validation plan for ESA's Sentinel-1 mission. From 2012 to 2016 on behalf of the European Space Agency (ESA), he was also responsible for conducting DLR's independent calibration of both satellites Sentinel-1A and Sentinel-1B. Under his leadership, the DLR SAR Calibration Center has been developed and established for efficient and accurate calibration of complex spaceborne SAR missions, including a new generation of remote controlled reference targets developed in-house, various evaluation tools based on precise algorithms for performance analysis and product quality control, the maintenance and operation of DLR's extended calibration site located in South Germany and the execution of comprehensive calibration campaigns. His major research interest includes the development of innovative and efficient calibration methods. Dr. Schwerdt received the Der Deutsche Gründerfonds Award in 1997 for establishing an enterprise of manufacturing electro-optical field sensors under the patronage of the German Federal Minister for Science and Research.